Mathematical and Computational Applications

MDPI

Article

Assessment of Local Radial Basis Function Collocation Method for Diffusion Problems Structured with Multiquadrics and Polyharmonic Splines

Izaz Ali [1], Umut Hanoglu [1,2], Robert Vertnik [3] and Božidar Šarler [1,2,*]

[1] Faculty of Mechanical Engineering, University of Ljubljana, 1000 Ljubljana, Slovenia; izaz.ali@fs.uni-lj.si (I.A.); umut.hanoglu@imt.si (U.H.)
[2] Institute of Metals and Technology, 1000 Ljubljana, Slovenia
[3] Štore Steel Podjetje za Proizvodnjo Jekel, d.o.o., 3220 Štore, Slovenia; robert.vertnik@fs.uni-lj.si
* Correspondence: bozidar.sarler@fs.uni-lj.si

Abstract: This paper aims to systematically assess the local radial basis function collocation method, structured with multiquadrics (MQs) and polyharmonic splines (PHSs), for solving steady and transient diffusion problems. The boundary value test involves a rectangle with Dirichlet, Neuman, and Robin boundary conditions, and the initial value test is associated with the Dirichlet jump problem on a square. The spectra of the free parameters of the method, i.e., node density, timestep, shape parameter, etc., are analyzed in terms of the average error. It is found that the use of MQs is less stable compared to PHSs for irregular node arrangements. For MQs, the most suitable shape parameter is determined for multiple cases. The relationship of the shape parameter with the total number of nodes, average error, node scattering factor, and the number of nodes in the local subdomain is also provided. For regular node arrangements, MQs produce slightly more accurate results, while for irregular node arrangements, PHSs provide higher accuracy than MQs. PHSs are recommended for use in diffusion problems that require irregular node spacing.

Keywords: meshless method; polyharmonic splines; multiquadrics; augmentation; heat diffusion equation

Citation: Ali, I.; Hanoglu, U.; Vertnik, R.; Šarler, B. Assessment of Local Radial Basis Function Collocation Method for Diffusion Problems Structured with Multiquadrics and Polyharmonic Splines. *Math. Comput. Appl.* **2024**, *29*, 23. https://doi.org/10.3390/mca29020023

Academic Editors: Benny Y. C. Hon, Zhuojia Fu and Junpu Li

Received: 15 February 2024
Revised: 14 March 2024
Accepted: 15 March 2024
Published: 17 March 2024

1. Introduction

The numerical solution of partial differential equations (PDEs), such as the heat diffusion equation (HDE), is extensively used in science and engineering. The phenomenon of heat diffusion is essential in solids for understanding various material processing and engineering problems such as phase transformations, corrosion, creep, annealing, etc. [1–3]. The development of the finite element method (FEM) in the 1950s was a significant breakthrough in numerical analysis. Many developed FEM packages are commercially available to solve complicated engineering problems [4] and are widely used. However, FEM involves certain limitations/difficulties, for example, the challenges during mesh creation [4] such as time-consuming (re)meshing to create a polygonization on the boundary and/or its domain [5] and the shortcomings in the evaluation of some problems like the connectivity of the mesh, which is very complex in the case of large deformations. That is why the idea of replacing the mesh with nodes only came into being to resolve this type of complication. The methods, defined on the nodes only, without geometric elements between them, are nowadays known as meshfree or meshless methods [4], depending on the level of the mesh reduction. "A meshfree/meshless method is a technique used to establish a system of algebraic equations for the whole problem domain without using the predefined mesh for the domain discretization" [4]. Meshless methods have proven

highly effective in solving numerical problems and have experienced rapid growth and advancement in recent years [4,6–10].

The radial basis function collocation method (RBFCM) was first proposed by Kansa [11,12]; that is why it is also known as Kansa's method [5,11]. The Kansa method presented a novel approach to solving partial differential equations using scattered data points rather than regular grids. Kansa, in [11], utilized the well-known MQ as a radial basis function to solve parabolic, hyperbolic, and elliptic partial differential equations, and it was proven that the MQ is not only highly accurate but also more efficient than the finite difference scheme. This method has been used to solve successfully different problems using MQs as RBFs. For example, some of the notable publications concern diffusion problems [5], H-adaptive LRBFCM [13], LRBFCM for linear thermo-elasticity in two dimensions [14], an equivalent PDE-based stabilization of strong-form meshless methods applied to advection-dominated problems [15], the simulation of laminar backwards-facing step flow under a magnetic field with explicit LRBFCM [16], and multi-pass hot-rolling simulation [17]. The MQ produces good results compared to the FDM [5], but the method is sensitive to the selection of the shape parameter [5]. Several methods have been introduced to select a suitable shape parameter [18,19]. However, this selection increases computational time because the process must be performed depending on the considered case. In this research, a more comprehensive study, compared to [5], is carried out for the selection of shape parameters for various node densities.

Orthogonal decomposition–radial basis function-generated finite difference (POD-RBF-FD) is used in solving three nonlinear partial differential equations in biology [20], demonstrating phenomena like blowing-up, pattern formation, and bacterial aggregations on surfaces. RBF-FD is used in study [21] to solve the time-dependent partial differential equations describing prostate tumor growth, demonstrating its effectiveness without requiring adaptivity. The localized singular boundary method (LSBM) for solving Laplace and Helmholtz equations in 2D arbitrary domains demonstrates improved efficiency and accuracy compared to traditional methods through various numerical examples [22]. A comprehensive overview of localized collocation schemes and their engineering applications is discussed in [23], showcasing their versatility in solving complex problems such as wave propagation analysis, phononic crystals, and heat conduction issues.

In recent years, the PHS kernel [24] has become popular because it does not require the time-consuming search for an optimal shape parameter, unlike the MQs. In RBF approaches, this feature of PHSs plays an essential role in more simple studies of convergence, stability, and accuracy [25,26]. According to [24], the convergence rate of the method using PHSs can be controlled with the highest order of augmentation monomials, meaning the higher the polynomial degree, the better the convergence rate, but it will also require larger subdomains and, as a result, more computation time. Many tests and experiments have recently been performed using PHS, such as the solidification of pure materials, solidification of binary alloys, phase-field modelling of solidification [27], an improved local radial basis function method for solving small-strain elasto-plasticity [28], a hybrid radial basis function finite difference method for modeling two-dimensional thermo-elasto-plasticity [29], and its application to the metallurgical cooling bed problem [30]. An application of PHSs to a real-world problem can be seen in the study of the reduction in discretization-induced anisotropy in the phase-field modeling of dendritic growth via the meshless approach [31]. One of the critical features of the PHS is that it can produce a highly accurate solution without spending time on choosing an optimal shape parameter and dealing with the numerical issues related to poor conditioning [32]. Some significant developments of PHS can be seen in [25] where they overcome the drawbacks of stability and accuracy due to Runge's phenomenon by increasing the nodes in the local subdomain two times the number of augmentation [25]. Furthermore, adding polynomials to PHS can achieve high convergence [24].

In this paper, we have investigated two cases, namely Case 1: the boundary value problem and Case 2: the initial value problem structured with MQs and polyharmonic

splines (PHSs) shape functions for solving the HDE. Previously, in [5], the same case studies were published using less dense nodes utilizing MQs as RBFs and comparing the results with the finite difference method (FDM). In [5], a convergence study was conducted for different node densities and arrangements. The method was shown to have higher accuracy than the traditional FDM and was performed through a straightforward, explicit process. In addition to this, it can easily cope with complicated geometry [5] and is scalable to handle large problems [33] efficiently. The method is also easy to understand and implement and can be extended to tackle other partial differential equations.

This study extends the findings in [5] by applying PHS and MQ radial basis functions to diffusion problems for different node arrangements and node densities, respectively. The novelty of this paper is that we have additionally evaluated the effects of the shape parameter, scaling factor in MQ, augmentation, scattering of the nodes, and number of nodes in the local subdomain, which were not discussed in the previous study [5].

The rest of the paper is structured as follows: Section 2 explains the materials and methods used in this article, representing the governing equation, solution procedure, definition of the shape functions, implementation of the boundary conditions, stability criterion of the explicit Euler method, and a brief introduction to the numerical examples, with the respective analytical solutions, namely, Case 1: the boundary value problem and Case 2: the initial value problem. Section 3 presents the results of the numerical examples with different parametric studies, and lastly, Section 4 presents a discussion of the results and the conclusions of this research study.

2. Materials and Methods

2.1. Governing Equation

We consider the solution of the diffusion equation in a two-dimensional (2D) domain Ω with a boundary Γ

$$\rho c \frac{\partial}{\partial t} T = k \nabla^2 T \,, \tag{1}$$

where T is the temperature, t is the time, ρ is the density, c is the specific heat, and k is the thermal conductivity. All material properties are considered constant. We seek the solution to the problem for $T(\mathbf{p}, t_0 + \Delta t)$, where $\mathbf{p} = p_x \mathbf{i}_x + p_y \mathbf{i}_y$ are the position vector, $\mathbf{i}_x, \mathbf{i}_y$ the base vectors, and p_x, p_y the coordinates of the 2D Cartesian coordinate systems. t_0 represents the initial time and Δt a positive time increment. Equation (1) is subject to the following initial condition:

$$T(\mathbf{p}, t_0) = T_0(\mathbf{p}); \ \mathbf{p} \in \Omega + \Gamma \,, \tag{2}$$

where T_0 is the initial temperature, and the Neumann-, Dirichlet-, and Robin-type boundary conditions at the not necessarily connected boundary segments are Γ^D, Γ^N, and Γ^R. These boundary conditions are defined at $\mathbf{p} \in \Gamma = \Gamma^D \cup \Gamma^N \cup \Gamma^R$ with outward normal $\mathbf{n}_\Gamma$, heat transfer coefficient h and reference temperature T_{ref} as

$$T = \Gamma^D; \ \mathbf{p} \in \Gamma^D \,, \tag{3}$$

$$-k \frac{\partial T}{\partial \mathbf{n}_\Gamma} = \Gamma^N; \ \mathbf{p} \in \Gamma^N \,, \tag{4}$$

$$-k \frac{\partial T}{\partial \mathbf{n}_\Gamma} = h\left(T - T_{ref}\right); \ \mathbf{p} \in \Gamma^R \,. \tag{5}$$

2.2. Solution Procedure

The solution to the heat diffusion problem with different types of boundary conditions is based on the strong-form local collocation meshless method with subdomains shown schematically in Figure 1.

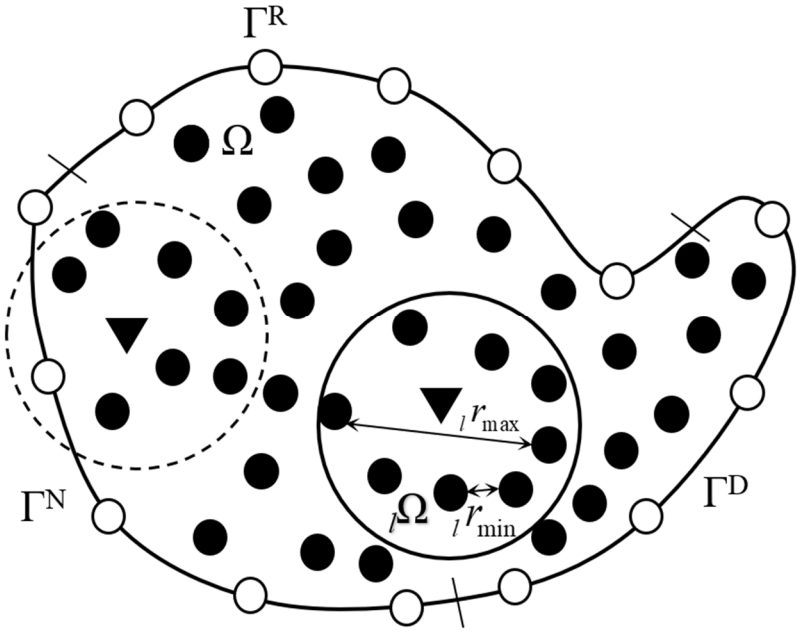

Figure 1. Scheme of the domain Ω with boundary conditions weighted at Γ^D, Γ^R, and Γ^N. The solid and empty circles show the interior and boundary nodes, respectively. The solid circular line shows the limits of the local sub-domain ${}_l\Omega$ containing nine interior nodes. In contrast, a dashed circular line represents another local sub-domain, containing a boundary node and eight interior nodes, whereas the solid triangle shows the central node. ${}_l r_{\max}$ and ${}_l r_{\min}$ are the maximum and minimum distance between any node in the subdomain l, respectively.

The forward Euler explicit formula is used to approximate the time derivative of temperature.

$$\frac{\partial}{\partial t}T \approx \frac{T - T_0}{\Delta t}, \tag{6}$$

And, Equation (1) becomes

$$T = T_0 + \Delta t \frac{k}{\rho c}\nabla^2 T_0 . \tag{7}$$

The system of equations for determining the unknown coefficients of collocation with the RBFs of an assumed function T with known values in the subdomain l with nodes ${}_l\mathbf{p}_n;\ n = 1, 2, ..., {}_lN$ at the respective subdomain ${}_l\Omega$, along with the polynomial augmentation, can be written as

$$T({}_l\mathbf{p}_n) = \sum_{k=1}^{{}_lN} {}_l\omega_k({}_l\mathbf{p}_n)\,{}_l\alpha_k + \sum_{k=1}^{{}_lN_{aug}} {}_lp_k({}_l\mathbf{p}_n)\,{}_l\alpha_{{}_lN+k} = \sum_{k=1}^{{}_lN+{}_lN_{aug}} {}_l\psi_k({}_l\mathbf{p}_n)\,{}_l\alpha_k , \tag{8}$$

with ${}_l\omega_k$ standing for the shape functions, and ψ consists of the shape functions (ω) and polynomials (p), while ${}_l\alpha_k$ represents the coefficients of the shape function with polynomials. The total number of nodes is $N = N_\Omega + N_\Gamma$, where N_Ω represents the number of nodes in the domain, and N_Γ represents the nodes positioned at the boundaries, whereas ${}_lN$ is the number of nodes in the subdomain l. In Equation (8), the augmented

polynomials are defined by ${}_l p_k$, and ${}_l\mathbf{p}$ stands for the central node of the subdomain. The number of augmentation monomials is defined as [28]

$$N_{aug} = \frac{(P + N_{\dim})!}{P! N_{\dim}!}, \tag{9}$$

where P is the order of the augmentation monomials, and $N_{\dim}$ is the number of dimensions. In this study, we are using $P = 0$ for MQs and $P = 2$ for PHSs, with $N_{\dim} = 2$ which yields $N_{aug} = 1, 6$, respectively. The polynomials for $N_{aug} = 1$ are defined as ${}_l p_1 = 1$, and $N_{aug} = 6$ is defined as ${}_l p_1 = 1, {}_l p_2 = x, {}_l p_3 = y, {}_l p_4 = x^2, {}_l p_5 = xy, {}_l p_6 = y^2$.

The collocation matrix should be non-singular to solve a square system of linear equations for the coefficients ${}_l\alpha_n$. We can rewrite Equation (8) in a vector–matrix form as follows:

$${}_l\underline{\boldsymbol{\Psi}}\,{}_l\boldsymbol{\alpha} = {}_l\mathbf{T};\ {}_l\underline{\Psi}_{kn} = {}_l\psi_k\left({}_l\mathbf{p}_n\right),\ {}_lT_n = T\left({}_l\mathbf{p}_n\right), \tag{10}$$

Together with the augmentation, according to Equation (8), our system is

$$\underbrace{\begin{bmatrix} {}_l\omega_1({}_lr_1) & {}_l\omega_2({}_lr_1) & \cdots & {}_l\omega_{{}_lN}({}_lr_1) & {}_lp_1({}_lr_1) & \cdots & {}_lp_{N_{aug}}({}_lr_1) \\ {}_l\omega_1({}_lr_2) & {}_l\omega_1({}_lr_2) & \cdots & {}_l\omega_{{}_lN}({}_lr_2) & {}_lp_1({}_lr_2) & \cdots & {}_lp_{N_{aug}}({}_lr_2) \\ \vdots & \vdots & \ddots & \vdots & \vdots & \ddots & \vdots \\ {}_l\omega_1({}_lr_{{}_lN}) & {}_l\omega_2({}_lr_{{}_lN}) & \cdots & {}_l\omega_N({}_lr_{{}_lN}) & {}_lp_1({}_lr_{{}_lN}) & \cdots & {}_lp_{N_{aug}}({}_lr_{{}_lN}) \\ {}_lp_1({}_lr_1) & {}_lp_1({}_lr_2) & \cdots & {}_lp_1({}_lr_{{}_lN}) & 0 & \cdots & 0 \\ \vdots & \vdots & \ddots & \vdots & \vdots & \ddots & \vdots \\ {}_lp_{N_{aug}}({}_lr_1) & {}_lp_{N_{aug}}({}_lr_2) & \cdots & {}_lp_{N_{aug}}({}_lr_{{}_lN}) & 0 & \cdots & 0 \end{bmatrix}}_{{}_l\underline{\boldsymbol{\Psi}}} \underbrace{\begin{bmatrix} {}_l\alpha_1 \\ {}_l\alpha_2 \\ \vdots \\ {}_l\alpha_{{}_lN} \\ {}_l\alpha_{{}_lN+1} \\ \vdots \\ {}_l\alpha_{{}_lN+N_{aug}} \end{bmatrix}}_{{}_l\boldsymbol{\alpha}} = \underbrace{\begin{bmatrix} {}_lT_1 \\ {}_lT_2 \\ \vdots \\ {}_lT_{{}_lN} \\ 0 \\ \vdots \\ 0 \end{bmatrix}}_{{}_l\mathbf{T}}. \tag{11}$$

In Equation (11), the unknown coefficients ${}_l\boldsymbol{\alpha}$ can be computed by solving the system of Equation (10).

$${}_l\boldsymbol{\alpha} = {}_l\underline{\boldsymbol{\Psi}}^{-1}\,{}_l\mathbf{T}, \tag{12}$$

By plugging the calculated coefficients ${}_l\boldsymbol{\alpha}$, i.e., Equation (12), into the collocation equation, i.e., Equation (8), for each subdomain, we can express the temperature and its first and second derivatives as

$$T(\mathbf{p}) = \sum_{k=1}^{{}_lN+N_{aug}} {}_l\psi_k(\mathbf{p}) \sum_{n=1}^{{}_lN} {}_l\underline{\Psi}^{-1}_{kn}\,{}_lT_{0n}, \tag{13}$$

$$\frac{\partial}{\partial p_\varsigma} T(\mathbf{p}) = \sum_{k=1}^{{}_lN+N_{aug}} \frac{\partial}{\partial p_\varsigma} {}_l\psi_k(\mathbf{p}) \sum_{n=1}^{{}_lN} {}_l\underline{\Psi}^{-1}_{kn}\,{}_lT_{0n};\ \varsigma = x, y, \tag{14}$$

$$\frac{\partial^2}{\partial p_\varsigma^2} T(\mathbf{p}) = \sum_{k=1}^{{}_lN+N_{aug}} \frac{\partial^2}{\partial p_\varsigma^2} {}_l\psi_k(\mathbf{p}) \sum_{n=1}^{{}_lN} {}_l\underline{\Psi}^{-1}_{kn}\,{}_lT_{0n};\ \varsigma = x, y. \tag{15}$$

The explicit discretization of Equation (7) is

$$T_l = T_{0l} + \frac{\Delta t k}{\rho c}\left[\sum_{k=1}^{{}_lN+N_{aug}} \frac{\partial^2}{\partial p_x^2} {}_l\psi_k(\mathbf{p}_l) \sum_{n=1}^{{}_lN} {}_l\underline{\Psi}^{-1}_{kn}\,{}_lT_{0n} + \sum_{k=1}^{{}_lN+N_{aug}} \frac{\partial^2}{\partial p_y^2} {}_l\psi_k(\mathbf{p}_l) \sum_{n=1}^{{}_lN} {}_l\underline{\Psi}^{-1}_{kn}\,{}_lT_{0n} \right]. \tag{16}$$

This study uses ${}_lN = 5$, ${}_lN = 9$, ${}_lN = 13$, and ${}_lN = 25$ nodes in the local subdomain, as shown in Figure 2. However, this article does not discuss using PHS with five nodes in the local subdomain because it does not produce any results since the number of

polynomials is more than that of the number of nodes in the local subdomain, which will result in a singular matrix.

The schematic representation of the local subdomains for regular node distribution (RND) is shown in Figure 2. Conversely, for quasi-uniform node distribution (QUND), the subdomain is defined by searching for the nearest neighbors until the required number at the nodes is set.

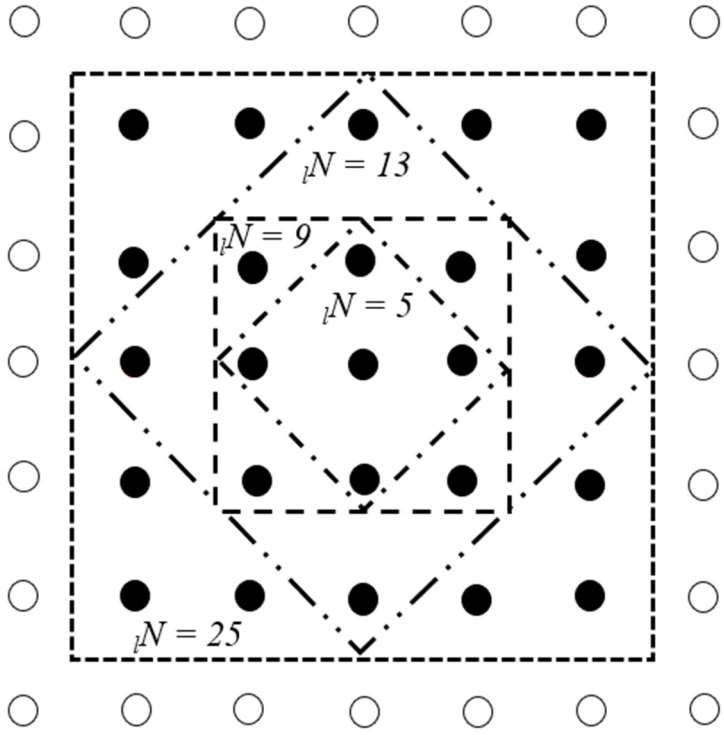

Figure 2. Local sub-domain scheme for RND with ${}_lN = 5, {}_lN = 9, {}_lN = 13, {}_lN = 25$. Solid and empty circles denote the inner and boundary nodes, respectively.

2.3. Definition of the Shape Functions

In this article, we have compared the scaled and unscaled MQs; the general equation for the scaled MQ used in this study is [5]

$$ {}_l\omega_k(\mathbf{p}) = \left[{}_l r_k^2(\mathbf{p}) + c^2 \, {}_l r_{\max}^2 \right]^{1/2}; \; {}_l r_k^2 = (\mathbf{p} - {}_l\mathbf{p}_k) \cdot (\mathbf{p} - {}_l\mathbf{p}_k), \tag{17} $$

where c represents the dimensionless shape parameter. The scaling parameter ${}_l r_{\max}^2$ is used for scaling the shape parameter and is set to the maximum nodal distance in the local subdomain.

$$ {}_l r_{\max}^2 = \max {}_l r_m^2 \left({}_l\mathbf{p}_n \right); \; m, n = 1, 2, ..., {}_lN. \tag{18} $$

In Section 3.1.6, a comparison of scaled and unscaled MQs is presented, where the unscaled MQ can be achieved by putting ${}_l r_{\max}$ equal to 1.

The involved first- and second-order derivatives of the scaled MQ for Equation (17) are given in Equations (19)–(22).

$$ \frac{\partial}{\partial p_x} {}_l\omega_k(\mathbf{p}) = \frac{p_x - {}_l p_{kx}}{\left({}_l r_k^2 + c^2 \, {}_l r_{\max}^2 \right)^{1/2}}, \tag{19} $$

$$\frac{\partial}{\partial p_y}{}_l\omega_k(\mathbf{p}) = \frac{p_y - {}_l p_{ky}}{\left({}_l r_k^2 + c^2\,{}_l r_{\max}^2\right)^{1/2}}, \tag{20}$$

$$\frac{\partial^2}{\partial p_x^2}{}_l\omega_k(\mathbf{p}) = \frac{\left(p_y - {}_l p_{ky}\right)^2 + c^2\,{}_l r_{\max}^2}{\left({}_l r_k^2 + c^2\,{}_l r_{\max}^2\right)^{3/2}}, \tag{21}$$

$$\frac{\partial^2}{\partial p_y^2}{}_l\omega_k(\mathbf{p}) = \frac{\left(p_x - {}_l p_{kx}\right)^2 + c^2\,{}_l r_{\max}^2}{\left({}_l r_k^2 + c^2\,{}_l r_{\max}^2\right)^{3/2}}, \tag{22}$$

while the derivatives of the unscaled MQ can be achieved by putting ${}_l r_{\max}$ equal to 1.

The general equation for the PHS is

$${}_l\omega_k(\mathbf{p}) = \left[\frac{{}_l r_k(\mathbf{p})}{{}_l r_0}\right]^n, \quad {}_l r_k = (\mathbf{p} - {}_l\mathbf{p}_k) \quad n = 1,3,5.....,\tag{23}$$

where ${}_l r_0$ is the scaling parameter, and the first- and second-order derivatives of the PHS are given in Equations (24)–(27).

$$\frac{\partial}{\partial p_x}{}_l\omega_k(\mathbf{p}) = \frac{n\left[{}_l r_k^{\frac{n-2}{2}}(\mathbf{p})\left(p_x - {}_l p_{kx}\right)\right]}{{}_l r_0^{2n}}, \tag{24}$$

$$\frac{\partial}{\partial p_y}{}_l\omega_k(\mathbf{p}) = \frac{n\left[{}_l r_k^{\frac{n-2}{2}}(\mathbf{p})\left(p_y - {}_l p_{ky}\right)\right]}{{}_l r_0^{2n}}, \tag{25}$$

$$\frac{\partial^2}{\partial p_x^2}{}_l\omega_k(\mathbf{p}) = \frac{n(n-2)\left(p_x - {}_l p_{kx}\right)^2\,{}_l r_k^{\frac{1}{2}}(\mathbf{p}) + n\,{}_l r_k^{\frac{n-2}{2}}(\mathbf{p})}{{}_l r_0^{2n}}, \tag{26}$$

$$\frac{\partial^2}{\partial p_y^2}{}_l\omega_k(\mathbf{p}) = \frac{n(n-2)\left(p_y - {}_l p_{ky}\right)^2\,{}_l r_k^{\frac{1}{2}}(\mathbf{p}) + n\,{}_l r_k^{\frac{n-2}{2}}(\mathbf{p})}{{}_l r_0^{2n}}, \tag{27}$$

where n is the (odd) power of the PHS, and in this study, we have used $n = 5$. It has been shown in [24] that the polynomial degree controls the convergence rate under high node refinement, not the PHS. Still, the solvency of the interpolation for $n = 5$ is ensured with the augmentation of the second-order monomials.

The scaling parameter ${}_l r_0$ represents the average distance and is calculated in the following way:

$${}_l r_0 = \sqrt{\sum_{k=2}^{{}_l N} \frac{{}_l r_k^{\,2}}{{}_l N - 1}}, \quad {}_l r_k^2 = ({}_l\mathbf{p} - {}_l\mathbf{p}_k)\cdot({}_l\mathbf{p} - {}_l\mathbf{p}_k), \tag{28}$$

where the nodes other than the central node ${}_l\mathbf{p}$ in the subdomain l is denoted as ${}_l\mathbf{p}_k$.

2.4. Implementation of the Boundary Conditions

The solution to both problems follows the following four steps.

In the first step, the derivatives at the initial temperature are calculated from the known values of the nodes in the domain by setting the initial conditions in the domain and boundary nodes.

In the second step, the new values for ${}_lT_n$ are calculated at $t_0 + \Delta t$ in the domain nodes using Equation (16).

In the third step, the discretization of the involved three types of boundary conditions is

$$\sum_{k=1}^{{}_lN+N_{aug}} {}_l\psi_k\left({}_l\mathbf{p}_n\right){}_l\alpha_k = {}_l\Gamma^D, \tag{29}$$

$$-k\sum_{k=1}^{{}_lN+N_{aug}} \frac{\partial}{\partial \mathbf{n}_\Gamma}{}_l\psi_k\left({}_l\mathbf{p}_n\right){}_l\alpha_k = {}_l\Gamma^N, \tag{30}$$

$$-k\sum_{k=1}^{{}_lN+N_{aug}} \frac{\partial}{\partial \mathbf{n}_\Gamma}{}_l\psi_k\left({}_l\mathbf{p}_n\right){}_l\alpha_k = h\left({}_l\mathbf{p}_n\right)\left(\sum_{k=1}^{{}_lN+N_{aug}} {}_l\psi_k\left({}_l\mathbf{p}_n\right){}_l\alpha_k - T_{ref}\left({}_l\mathbf{p}_n\right)\right). \tag{31}$$

The boundary conditions can be applied by replacing a row of the neighboring boundary node in Equation (11) with the respective boundary conditions prescribed in Equations (29)–(31). The unknown values are calculated using Equation (16) with the help of the specified boundary conditions.

Finally, the calculated ${}_l\alpha_k$ from Equation (12) are then plugged into Equation (11) to find the unknown values of ${}_lT_n$ at the boundary where the Neuman or Robin boundary conditions are defined.

2.5. The Stability Criterion of the Explicit Euler Method

For the explicit Euler method, it is necessary to limit the timestep size. The maximum value for the timestep can be calculated as [34]

$$\Delta t = \frac{m_{\Delta t} r_{\min}^2}{D} \Rightarrow m_{\Delta t} = \frac{\Delta t D}{r_{\min}^2};\ D = \frac{k}{\rho c}, \tag{32}$$

where $m_{\Delta t}$ is the mesh Fourier number based on the timestep used in our simulations, $r_{\min}$ is the minimum node distance, and D denotes thermal diffusivity. The stability of the explicit Euler method is assured for $m_{\Delta t\min} \le 0.25$ [34] in the case of the finite difference method.

2.6. Numerical Implementation

The code is written in Fortran 2008 and compiled into a 64-bit executable with Intel Visual Fortran compiler (XE 19). The simulations are carried out using an Intel(R) Core(TM) i7-7700HQ processor. The same code elements have also been used in [14,15,19,35,36].

2.7. Numerical Examples

We are extending the previously published findings [5] by investigating the comparison of MQs with PHSs as RBFs. This research extensively explains the effects of a relatively large range of node densities, timestep, shape parameter, scaling of the MQ, number of the nodes in the subdomain, the effects of augmentation, and the irregularity of node arrangements in terms of the average error for a boundary value and initial value test cases. In addition, this research also demonstrates the selection of an optimal shape parameter for MQs to compare the best results of MQs with PHSs.

2.7.1. Case 1: Boundary Value Problem

The Case 1 problem is posed on a two-dimensional rectangular domain, as shown in Figure 3; the boundary conditions and material properties are the same as in [5] and are

given in Figure 3 and Table 1 below, whereas the respective node distributions are shown in Figure 4.

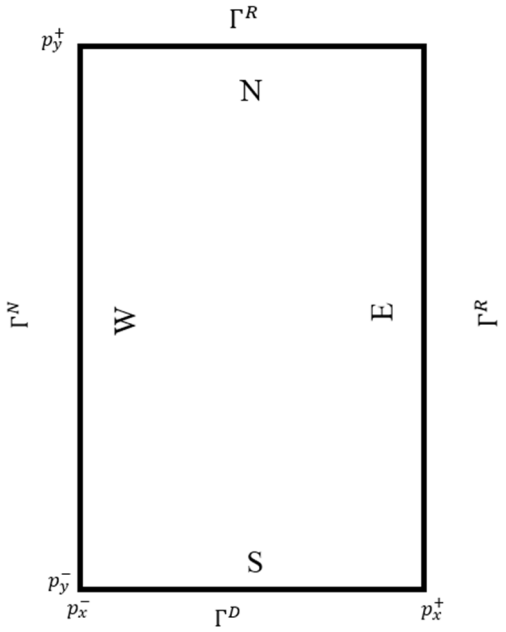

Figure 3. Scheme of Case 1 with geometry ($p_x^- = p_y^- = 0$ m, $p_x^+ = 0.6$ m, $p_y^+ = 1$ m) and boundary conditions.

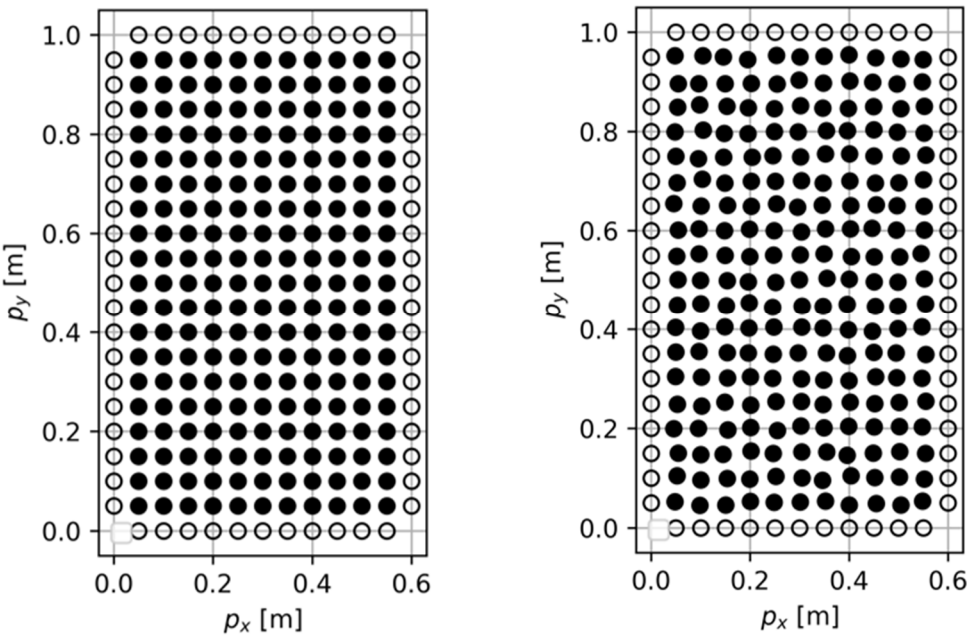

Figure 4. Case 1, RND and QUND with $N = 13 \times 21$ nodes. In regular node distribution, the $_{I}r_{\min}$ is 0.05 m and $_{I}r_{\max}$ is 0.1802 m, while for QUND, $_{I}r_{\min}$ is 0.0994 m, and the $_{I}r_{\max}$ is 0.1839 m.

Table 1. Material properties, boundary, and initial conditions used in Case 1 studies.

Material Property	Value
Density (ρ) [kg/m^3]	7850
Specific heat I [J/(kg K)]	460

Thermal conductivity (k) [W/(mK)]	52
Heat transfer coefficient (h) [W/(m²K)]	750
Reference temperature (T_{ref}) [°C]	0
Dirichlet boundary temperature (Γ^D) [°C]	100
Neuman boundary condition (Γ^N) [W/m²]	0

Analytical Solution

The steady-state analytical solution T_{ana} of Case 1 [5] is

$$T_{ana}\left(p_x, p_y\right) = 2hT_0 \sum_{i=1}^{\infty} \frac{\cos\beta_i x\left[\beta_i \cosh\beta_i\left(p_y^+ - p_y\right) + h\sinh\beta_i\left(p_y^+ - p_y\right)\right]}{\cos\beta_i p_x^+\left[\left(\beta_i^2 + h^2\right)p_x^+ + h\right]\left[\left(\beta_i \cosh\beta_i p_y^+ + h\sinh\beta_i p_y^+\right)\right]}, \quad (33)$$

where β_i represents the positive roots of the equation

$$\beta\tan\left[\beta\left(p_x^+ - p_x^-\right)\right] = h, \quad (34)$$

where the results of i, for boundary nodes (0.6 m, 0.1 m), (0.5 m, 1 m), (0.3 m, 0.5 m), and (0 m, 0.9 m) are shown in Figure 5, which shows that as we approach the south from the north, the number of terms required for a stable solution increases. Based on the results, it is concluded that $i \geq 20$ and, in this study, we have used $i = 100$.

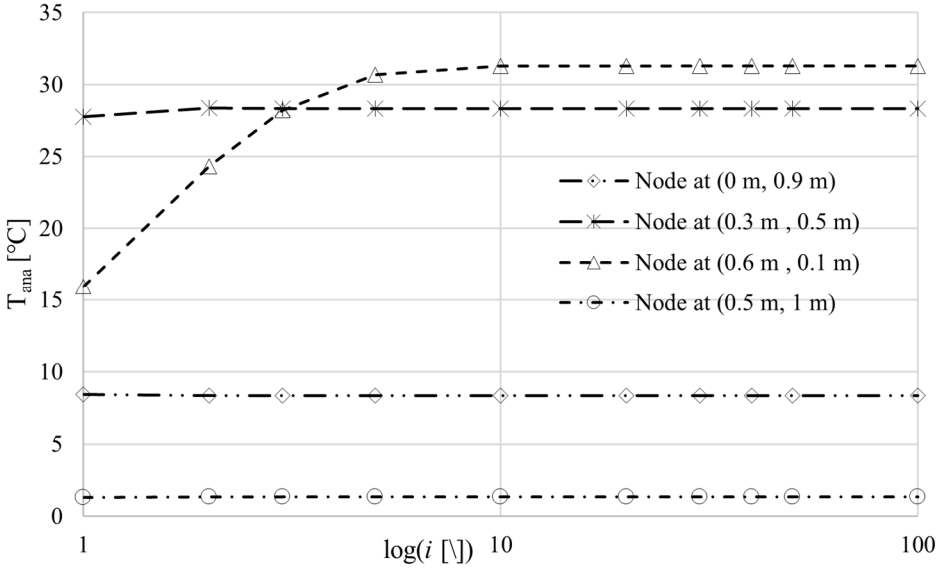

Figure 5. Case 1, convergence analysis of analytical solution as a function of the terms i used in the evaluation of Equation (33) for four different nodes, i.e., (0.6 m, 0.1 m), (0.5 m, 1 m), (0.3 m, 0.5 m), and (0 m, 0.9 m) of the rectangular geometry.

In order to compare the results, the analytical solution has been calculated for each node to find the absolute temperature error ε_{max} and average error ε_{avg} of the numerical solution at time t as follows [5]:

$$\varepsilon_{max}(t) = max\left|T\left(\mathbf{p}_n, t\right) - T_{ana}\left(\mathbf{p}_n\right)\right|; \quad n = 1, 2, ..., N, \quad (35)$$

$$\varepsilon_{avg}(t) = \sum_{n=1}^{N} \frac{1}{N}\left|T\left(\mathbf{p}_n, t\right) - T_{ana}\left(\mathbf{p}_n\right)\right|; \quad n = 1, 2, ..., N, \quad (36)$$

where T and T_{ana} define the numerical and the analytical solution, and $T\left(\mathbf{p}_n, t\right)$ stands for the steady-state solution.

The simulations are stopped when the steady state is achieved by satisfying the criterion

$$\max\left|T_n - T_{0n}\right| \le T_{\text{ste}}. \tag{37}$$

In all computational nodes, $\mathbf{p}_n; n = 1, 2, ..., N$. The parameter T_{ste} represents the steady-state convergence margin, which is chosen to be less than or equal to 10^{-6} °C in all the calculations in this paper. The analysis is stopped if the steady-state criterion is achieved or the calculation time exceeds the foreseen time of interest.

Some fixed values used throughout the simulations are given in Table 2, while the position of local nodes is shown in Figure 2.

Table 2. Fixed parameters used in the simulations of Case 1 studies.

RBF	PHS	MQ
Δt [s]	0.005	0.005
$_lN$	9	9
	13	13
	25	25
c	-	1
	-	8
	-	16
	-	32
	-	64
N_{aug}	6	1
Scattering factor (δ)	0.10	0.10
T_{ste} [°C]	10^{-6}	10^{-6}
Initial temperature (T_0) [°C]	100	100

Computational Parameters

In this study, the used node densities and their respective boundary and inner boundary nodes are given in Table 3. The simulations have been carried out for 9, 13, and 25 nodes in a subdomain.

Table 3. Node densities with boundary and domain nodes used in Case 1 studies.

Node's Arrangement	Total Number of Nodes (N)	Number of Boundary Nodes (N_Γ)	Number of Domain Nodes (N_Ω)
13 × 21	269	60	209
31 × 51	1577	156	1421
61 × 101	6157	316	5841
121 × 201	24,321	636	23,685
241 × 401	96,641	1276	95,365

It is well known that as the node density increases, the timestep should decrease for a stable solution, and according to Equation (32), for the most dense node arrangement ($N = 241\text{x}401$), we should choose a timestep below $\Delta t \le 1.08\times10^{-2}$ s. In order to be on the safe side, we have used a timestep of $\Delta t = 5\times10^{-3}$ s in all cases.

The minimum and used mesh Fourier numbers for Case 1 are presented in Table 4 below.

Table 4. Minimum and used mesh Fourier number for the stable solution of Case 1.

N	$m_{\Delta t \min}$	$m_{\Delta t}$	$r_{\min}$ **[m]**
241 × 401	0.25	0.116	0.002
121 × 201	0.25	0.029	0.005
61 × 101	0.25	0.00744	0.00984
31 × 51	0.25	0.00180	0.02000
13 × 21	0.25	0.00029	0.05000

Table 4 shows the minimum Fourier number values ($m_{\Delta t \min}$) for a stable solution and the values used for the Fourier number ($m_{\Delta t}$) based on the timestep Δt in our calculations. It is clear from Table 4 that we have used a permissive value for the Fourier number in our simulations.

2.7.2. Case 2: Initial Value Problem

The initial value problem is solved on a square geometry, with the boundary conditions shown in Figure 6 and the material properties given in Table 5 below. The respective node distribution is shown in Figure 7.

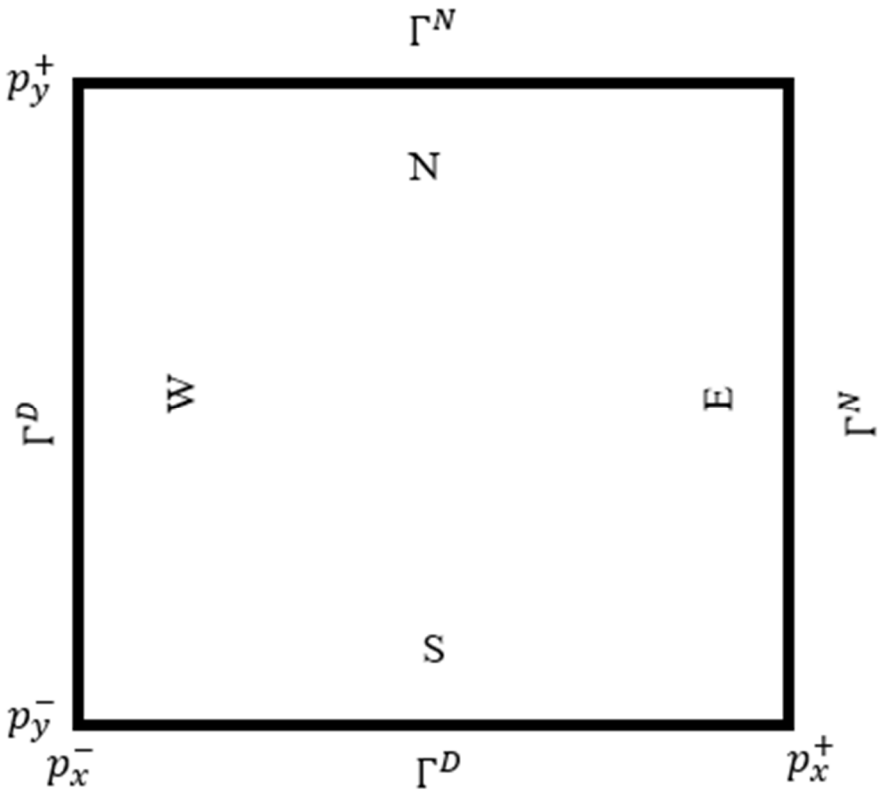

Figure 6. Scheme of Case 2 with geometry ($p_x^- = p_y^- = 0$ m 嬡 $p_x^+ = p_y^+ = 1$ m) and boundary conditions.

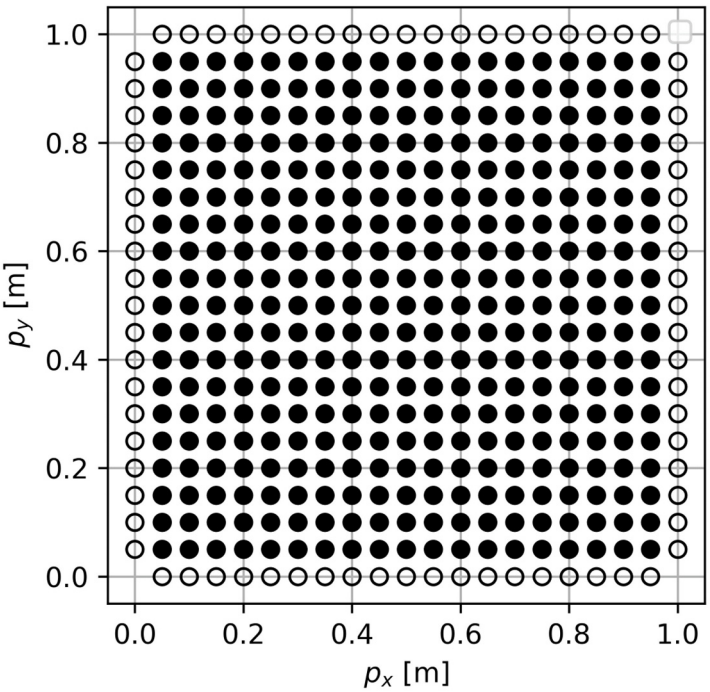

Figure 7. Case 2, regular nodes distribution is shown for $N = 21 \times 21$ and ${}_{l}N = 13$ node arrangement with ${}_{l}r_{\min}$ is 0.05 m and ${}_{l}r_{\max}$ is 0.18027 m, solid and empty circles representing the inner and boundary nodes respectively.

Table 5. Material properties used in Case 2 studies.

Material Property	Value
Density (ρ) [kg/m^3]	1
Specific heat (c) [J/(kg K)]	1
Thermal conductivity (k) [W/(mK)]	1
Initial temperature (T_0) [°C]	1

Analytical Solution

The analytical solution to the problem is given as [5]

$$T_{\text{ana}}\left(p_x, p_y, t\right) = T_{\text{ana}}\left(p_x, t\right) T_{\text{ana}}\left(p_y, t\right), \tag{38}$$

with

$$T_{\text{ana}}\left(p_\varsigma, t\right) = \frac{4}{\pi} \sum_{i=1}^{\infty} \frac{-1^i}{2i+1} \exp\left[-\frac{k\left(2i+1\right)^2 \pi^2 t}{4\rho c \left(p_\varsigma^+ - p_\varsigma^-\right)^2} \right] \cos\left[\frac{\left(2i+1\right)\pi\left(p_\varsigma - 1\right)}{2\left(p_\varsigma^+ - p_\varsigma^-\right)} \right]; \varsigma = x, y, \tag{39}$$

where some values of i for two different nodes at positions (0.5 m, 0.5 m) and (0.6 m, 0.9 m) at time 0.001, 0.1, and 1 s are given in Figure 8, and based on this, it is concluded that if $i \geq 30$, then the analytical solution will produce stable results, and in this study, we have used $i = 50$.

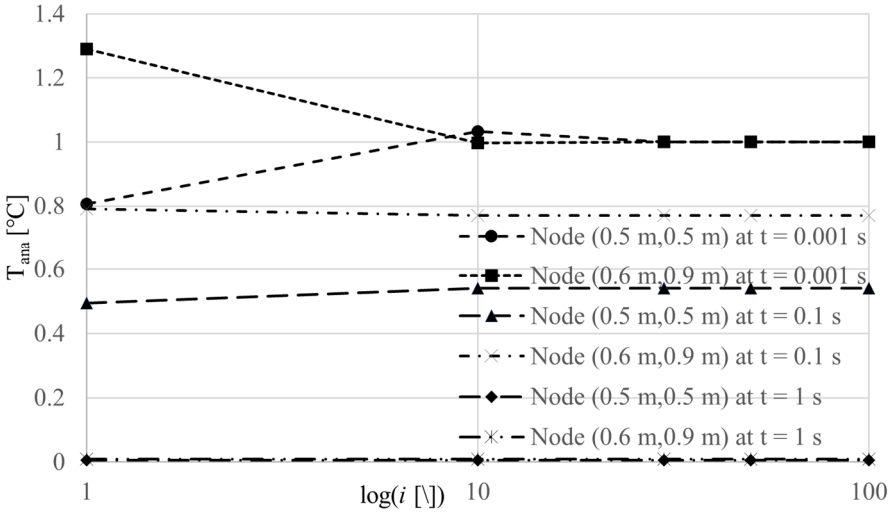

Figure 8. Case 2, convergence analysis of analytical solution as a function of the terms i used in evaluating Equation (39) for two nodes, i.e., at (0.5 m, 0.5 m) and (0.6 m, 0.9 m), of the square geometry for time t = 0.001 s, 0.1 s, and 1 s.

Some fixed values we used throughout the simulations are given in Table 6.

Table 6. Fixed parameters used for the simulations in Case 2 studies.

RBF	PHS	MQ
Δt [s]	10^{-6}	10^{-6}
t [s]	1	1
	0.1	0.1
	0.01	0.01
	0.001	0.001
$_lN$	-	5
	9	9
	13	13
	25	25
c	-	8
	-	16
	-	32
	-	64
N_{aug}	6	1

Computational Parameters

In this study, the used node densities and their respective boundary and inner boundary nodes for Case 2 studies are given in Table 7. The simulations have been carried out for 5, 9, 13, and 25 nodes in a subdomain.

Table 7. Node densities with boundary and domain nodes used in Case 2 studies.

Node's Arrangement	Total Number of Nodes (N)	Number of Boundary Nodes (N_Γ)	Number of Domain Nodes (N_Ω)
11 × 11	117	32	85
21 × 21	437	72	365
41 × 41	1677	152	1525
101 × 101	10197	392	9805

For Case 2 studies with the densest nodes (N =101×101), the timestep should be chosen below $\Delta t \le 2.5\times10^{-3}$, and we have used $\Delta t = 5\times10^{-6}$ s.

The minimum and used mesh Fourier numbers for Case 2 are presented in Table 8 below.

Table 8. Minimum and used mesh Fourier number for the stable solution of Case 2.

N	$m_{\Delta t\,\min}$	$m_{\Delta t}$	$r_{\min}$ **[m]**
11 × 11	0.25	0.00121	0.09090
21 × 21	0.25	0.00441	0.04761
41 × 41	0.25	0.01681	0.02439
101 × 101	0.25	0.102	0.00990

It is clear from Table 8 that we have used a permissive value for the Fourier number in our simulations.

3. Results

3.1. Results and Discussion for Case 1

In this section, we discuss the results of the simulations for different parameters and arrangements (RND and QUND) with MQs and PHSs. The simulations ran until the steady-state criterion of T_{ste} = 10⁻⁶ °C was reached.

3.1.1. Effects of Augmentation for MQ

As we know, in the case of PHS, if we increase the degree of the polynomial, the error reduces [24], but in the case of MQs, this is not always true. To assess the effects of augmentation on MQs, we ran test simulations by selecting different nodes in the local subdomain (${}_{l}N = 5,\ 9$ & 13). The augmentation effects are presented in terms of the difference in the average error based on the number of nodes in the local subdomain, as shown in Figures 9–11. Note that due to a very small difference between the results (which was hard to see clearly in a graph), we have decided to show the difference between two average errors in terms of percentage on the vertical axis of each graph.

The difference between the average errors and their percentage improvement is calculated as

$$\Delta\varepsilon_{\%} = \frac{\varepsilon_{avg,0} - \varepsilon_{avg,aug}}{\varepsilon_{avg,0}} 100\%, \quad aug = 1,3\,. \tag{40}$$

In Figure 9, it is shown that, for five nodes in the local subdomain, as we increase the number of augmentations from zero to one, it significantly affects denser node arrangement (about 40% for $N = 241\times401$). At the same time, it shows a relatively small effect on the less dense nodes, while it shows a very slight change in the results if we change the number of augmentations from 1 to 3. Another aspect we can see from Figures 9–11 is that as we increase the number of local nodes from 5 to 9 to 13, the percentage improvement in the average error drops. For 9 and 13 nodes in the local subdomain, increasing the augmentation from 0 to 3 decreases the accuracy, as described in [37,38] as well. It is also observed that for denser nodes, augmentation always improves the accuracy; however, in some cases, augmentation 1 gives the best results. Therefore, this article will use augmentation with a constant polynomial using MQs as RBFs for better accuracy and less computational time.

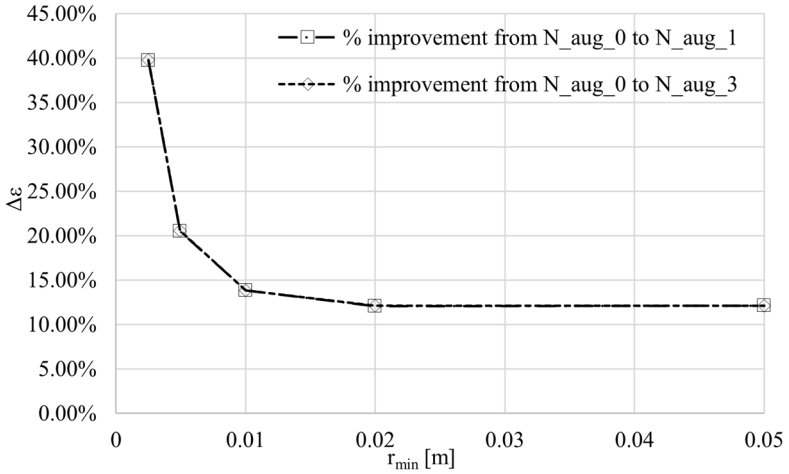

Figure 9. Case 1, the difference in % of the ε_{avg} as a function of the node distance for MQ with and without augmentation (RND, $c = 64$, $_{l}N = 5$).

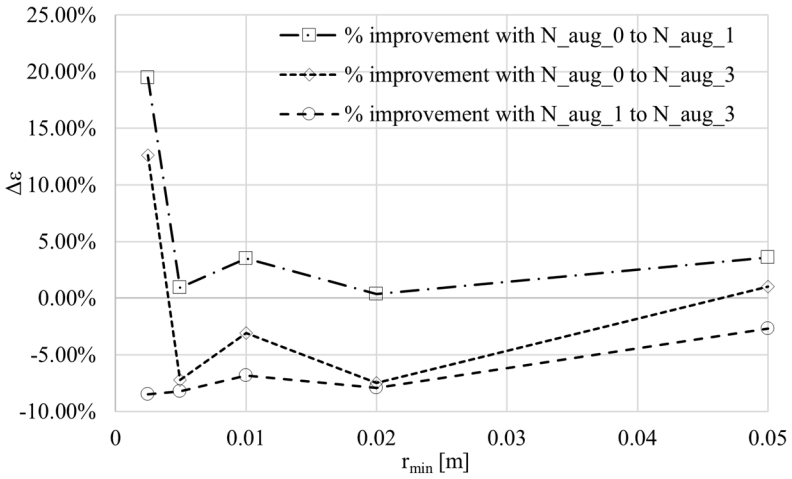

Figure 10. Case 1, improvement in % of the ε_{avg} as a function of the node distance for MQ with and without augmentation (RND, $c = 64$, $_{l}N = 9$).

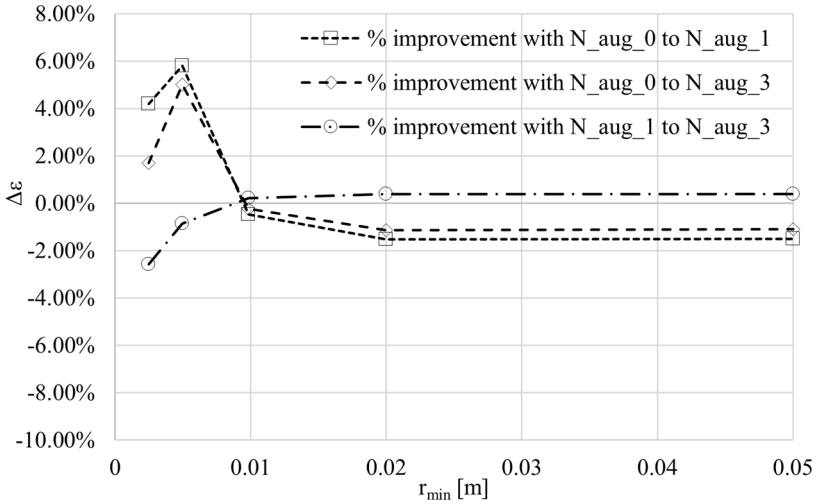

Figure 11. Case 1, improvement in % of the ε_{avg} as a function of the node distance for MQ with and without augmentation (RND, $c = 32$, $_{l}N = 13$).

3.1.2. Selection of an Optimal Shape Parameter for MQs

The PHS is a method free of shape parameters [24], while the MQ is a shape parameter-dependent method. In order to obtain a smaller average temperature error, we need to find an optimum shape parameter for MQs.

The shape parameter plays a vital role in converging the absolute average temperature error. That is why a suitable shape parameter selection is mandatory for MQs. In this paper, we show the effects of different shape parameters on the results of the average temperature error for 9, 13, and 25 nodes in the local subdomain.

Figure 12 shows the relation of the average error with different shape parameter values. For shape parameters 1 and 8, the convergence curve is not smooth when increasing the number of total nodes while keeping 9 nodes in the local subdomain. Figure 12 shows a smooth converging curve for shape parameters 16, 32, and 64. Some simulations for different shape parameters are shown in Figure 13. It is shown that the results will not change if we choose a shape parameter equal to or greater than 50 with nine nodes in the local subdomain for this specific case. We have used 64 as the optimal shape parameter with nine nodes in the local subdomain. We obtain a constant value of the absolute average temperature error with a shape parameter equal to 64, as shown in Figure 13.

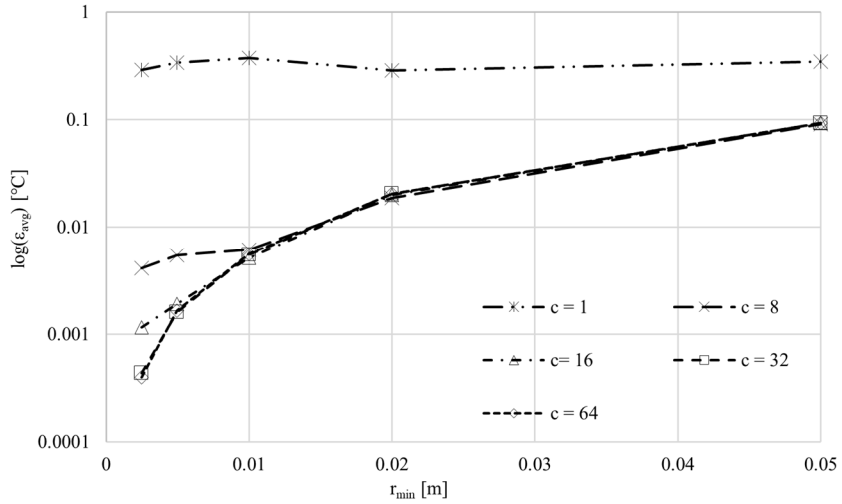

Figure 12. Case 1, MQ, ε_{avg} as a function of node distance calculated for five different shape parameters (RND, $N_{aug}=1$, $_{l}N=9$).

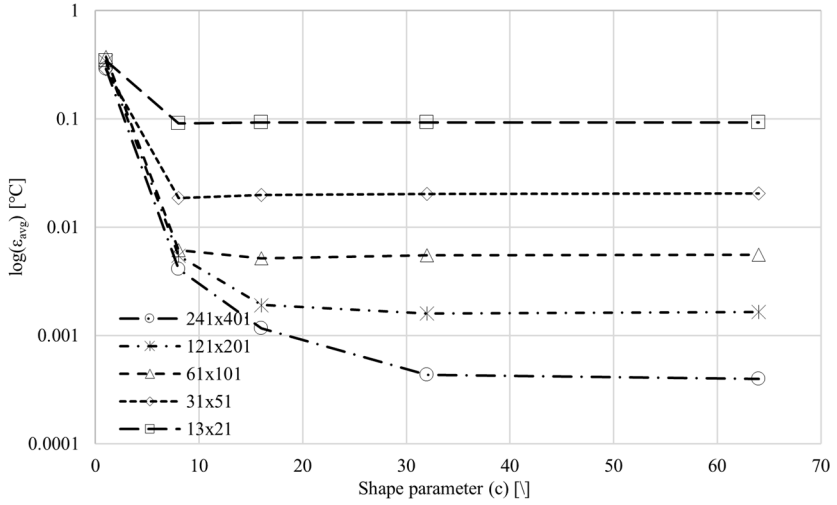

Figure 13. Case 1, MQ, ε_{avg} as a function of shape parameter (RND, $N_{aug}=1$, $_{l}N=9$).

Increasing the number of nodes in the local subdomain requires a smaller shape parameter to obtain accurate results. Figure 14 shows a relation between the average error and shape parameter. It is demonstrated that by increasing the shape parameter, the error decreases, with an increase in the node density. In contrast, this direct relation between the shape parameter and the average error is valid up to a certain value of the shape parameter; when the shape parameter exceeds that particular value (32 in this case), then the change in the error is negligible by increasing the shape parameter. This can be seen clearly in Figure 15. In the case of 13 nodes in the local subdomain, if we choose a shape parameter equal to or greater than 32, we will reach the critical value of the shape parameter, after which the results no longer change. Detailed research has been conducted to find the most suitable shape parameter for more accurate results while using 13 nodes in the local subdomain, shown in Figures 14 and 15. It is clear from Figure 15 that with 13 nodes in the local subdomain, if we choose a shape parameter equal to 32, then we will obtain the least absolute average temperature error.

Increasing the number of nodes in the local subdomain makes the MQ more sensitive to selecting the optimal shape parameter. For example, we have carried out some test simulations and found that the MQ for 25 nodes in the local subdomain is much more sensitive to the shape parameter. In our simulations, we could reach a maximum of $c = 2.43$ value for the shape parameter, above which the results diverge. At the same time, it shows the same trend in terms of accuracy, i.e., by increasing the shape parameter from 1 to 2.43, the average error decreases, which is similar in behavior to 9 and 13 nodes in the local subdomain. In contrast, we obtain diverging results if we use a value greater than 2.43 for the shape parameter in the case of 25 nodes in the local subdomain for the 241 × 401 node distribution. The discussion above shows that the critical point at which the shape parameter no longer affects the results is smaller for less dense nodes.

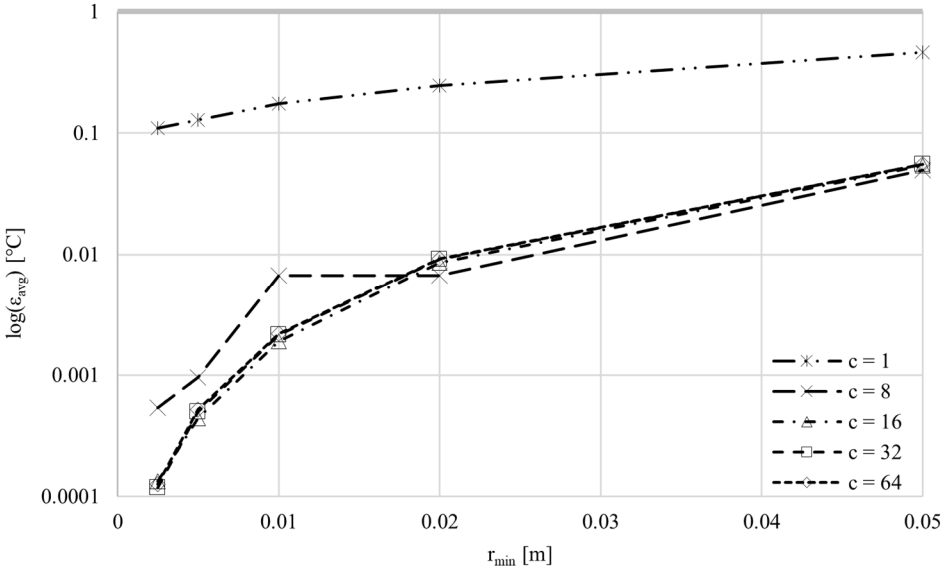

Figure 14. Case 1, MQ, ε_{avg} as a function of the node distance for different shape parameters (RND, $N_{aug} = 1$, $_{l}N = 13$).

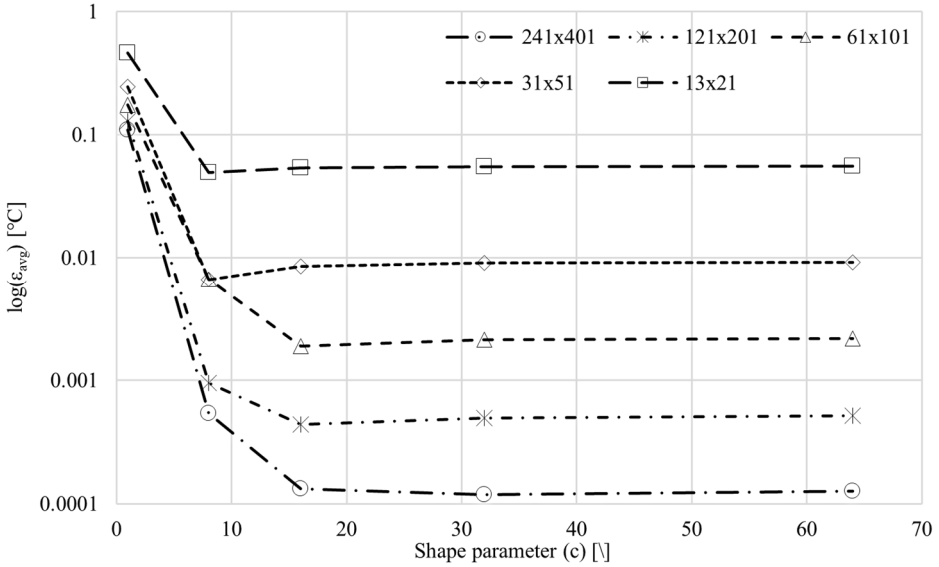

Figure 15. Case 1, MQ, ε_{avg} as a function of the shape parameter (RND, $N_{aug}=1$, $_{l}N=13$).

3.1.3. Effects of the Number of Nodes in the Local Subdomain on the Absolute Average Error for PHS and MQ

This section shows the effects of the number of nodes in the local subdomain for regular nodes of PHSs and MQs separately.

Figure 16 shows the average error for PHSs using different numbers of nodes in the local subdomain. The absolute average error decreases as we increase the number of nodes in the local subdomain from 9 to 13. If we further increase the number of nodes in the local subdomain to 25, then an increase in the error can be seen, as shown in Figure 16. The average error for 13 nodes in the local subdomain is the smallest, and thus, it is recommended that for RNDs, a selection of 13 nodes in the local subdomain would be a good choice when PHSs are used for solving complex problems.

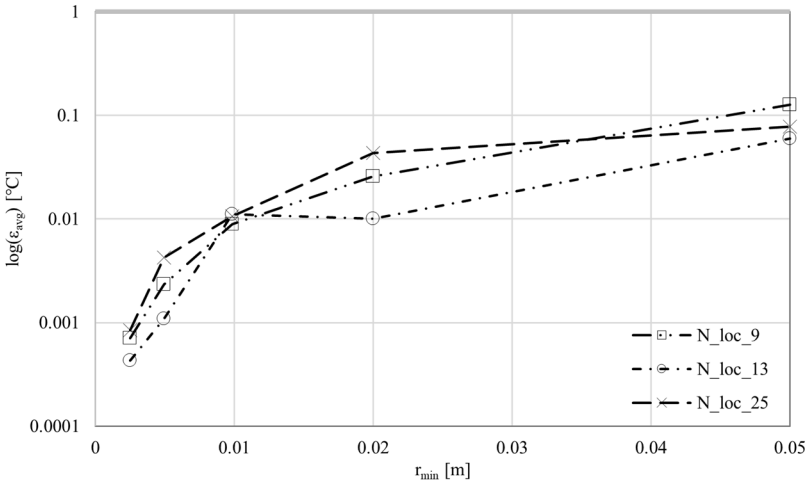

Figure 16. Case 1, PHS, ε_{avg} as a function of node distance for a different number of nodes in the local subdomain (RND, $N_{aug}=6$).

The selection of an optimum shape parameter is the most critical and challenging task for MQs, which is already discussed in Section 3.1.2. Figure 17 shows the average error for MQs using optimal shape parameters and different numbers of nodes in the local subdomain. This figure shows that we obtain more accurate results by increasing the

number of nodes in the local subdomain. Therefore, if we use a shape parameter equal to 32 and 13 nodes in the local subdomain, then the value for the average error for the highest denser nodes will be the smallest, while for the case of 25 nodes in the local subdomain, selecting an optimum shape parameter is very limited. We could choose a maximum of 2.43 as a shape parameter for 25 nodes in the local subdomain. Any value for a shape parameter greater than 2.43 for 25 nodes in the local subdomain will give diverging results using the same timestep.

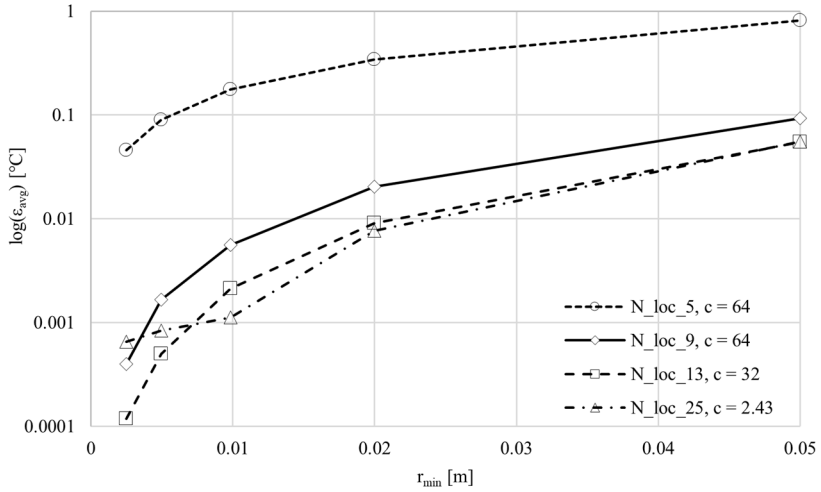

Figure 17. Case 1, MQ, ε_{avg} as a function node distance with a different number of nodes in the local subdomain and optimum shape parameter (RND, $N_{aug}=1$).

3.1.4. Comparison of MQs and PHSs Based on the Average Error

In this section, we present the accuracy of PHSs and MQs based on the smallest average error, as shown in Figure 18. It has been shown in the text earlier that both PHSs and MQs produce more accurate results for high denser nodes while using ${}_{l}N=13$. We compare the best results for both PHSs and MQs (in terms of the number of nodes in the local subdomain), and it can be concluded that PHSs and MQs show the same accuracy for a small number of total nodes. In contrast, in the case of a larger number of total nodes, MQs with 13 nodes in the local subdomain would be a good choice for higher accuracy, considering that an optimal shape parameter should be selected for MQs.

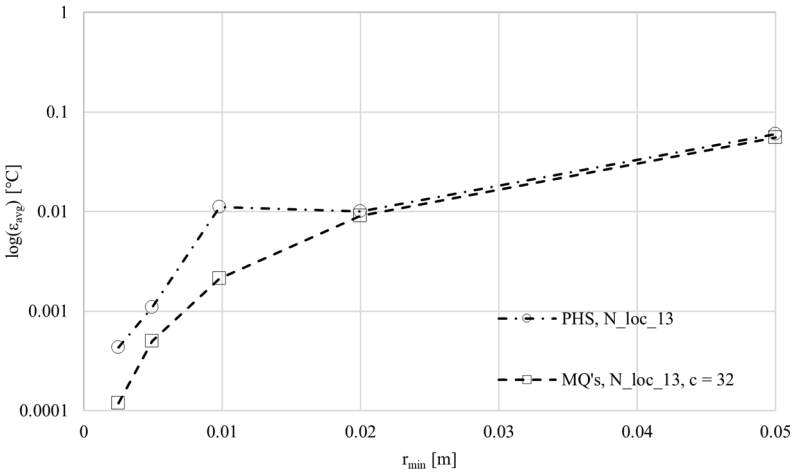

Figure 18. Case 1, ε_{avg} as a function of node distance (RND, MQ with $N_{aug}=1$, and PHS with $N_{aug}=6$).

3.1.5. Effects of Non-Uniformity of the Nodes

This section explores the maximum limit, up to which the results are converging, for the non-uniformity of the nodes based on the average error. Figure 4 shows the irregular node arrangements with $N = 13 \times 21$ node density; the QUNDs are generated in the domain by transforming the regular nodes in the following manner:

$$p_{n\varsigma(\text{nonuniform})} = p_{n\varsigma(\text{uniform})} + (2c_{\text{random}} - 1)\delta p_{n\varsigma(\text{uniform})}; \varsigma = x, y, \quad (41)$$

where c_{random} represents a random number $-1 \le c_{\text{random}} \le +1$, δ represents a scattering factor. Simulations with 9, 13, and 25 nodes in the local subdomain have been carried out to find a constant value of the scattering factor for all cases with different shape parameters on which the convergence can be achieved for the given problem, as shown in Figure 19. It has been shown that the range of selection for the scattering factor in the case of PHSs is longer than that of MQs. All values shown in Figure 19 are the possible range for the selection of the scattering factor for the present case; any value greater than those shown in Figure 19 will result in the divergence of the results. Figure 19 also shows that increasing the shape parameter for the MQ increases the accuracy but eventually decreases the range for selecting the scattering factor. Another aspect of Figure 19 is that increasing the number of nodes in the local subdomain also increases the range for selecting the scattering factor because of the wide range of subdomains. The PHS deals better with the scattering factor.

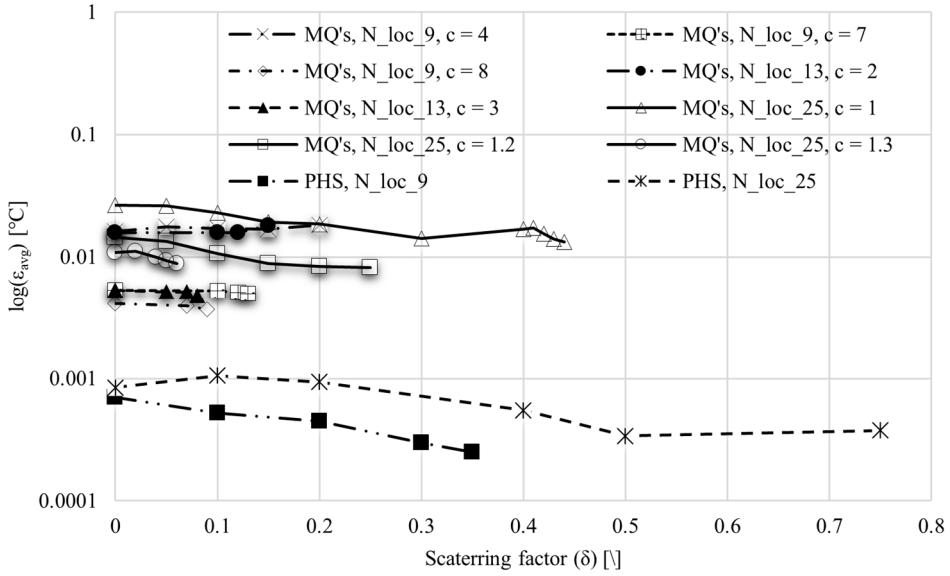

Figure 19. Case 1, ε_{avg} as a function of the scattering factor (δ) (QUND, $N = 241 \times 401$).

In the rest of the simulations, we fixed the scattering factor equal to 0.10 for both PHSs and MQs because, with this value, all the present study cases converge and produce good results. As shown in Figure 19, we conducted multiple tests to find the optimal shape parameters for QUND using MQs with different nodes in the local subdomain. All the simulations in this section use the optimal shape parameters. A comparison of the average temperature error with a different number of nodes in the local subdomain for PHSs can be seen in Figure 20; it is clear that 13 nodes in the local subdomain should be selected for better accuracy and smooth convergence.

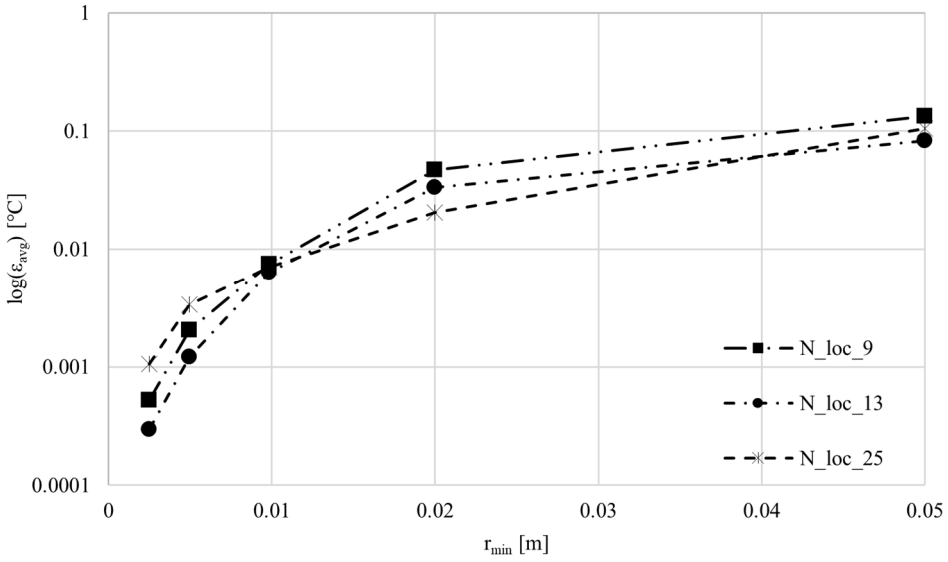

Figure 20. Case 1, PHS, ε_{avg} error as a function of the node distance for different ${}_{l}N$ (QUND, $\delta = 0.10$, $N_{aug} = 6$).

The average temperature error for MQs is shown in Figure 21. From this figure, we can say that with a scattering factor of 0.10, we should select nine nodes in the local subdomain and seven as the shape parameter. It should also be noted here that as we increase the number of nodes in the local subdomain, the range for the selection of the shape parameter decreases, while the range for the selection of the scattering factor increases.

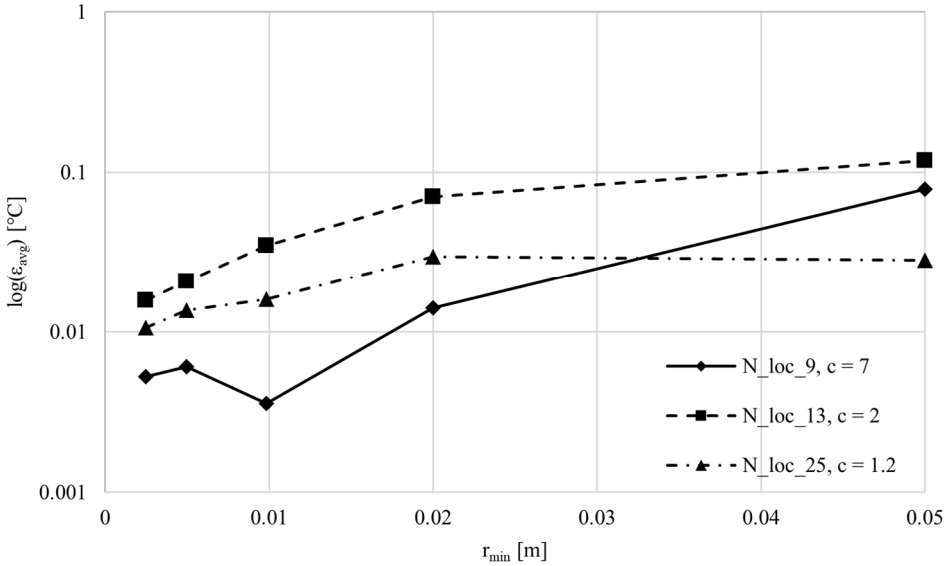

Figure 21. Case 1, MQ, ε_{avg} as a function of the node distance for different ${}_{l}N$ (QUND, $\delta = 0.10 \quad N_{aug} = 1$).

A comparison of the results for PHSs and MQs is shown in Figure 22; we can see that the MQ is a good choice for less dense nodes. However, as the total number of nodes increases, the PHS becomes an appropriate choice for calculating the average temperature error. The PHS has an advantage over the MQ by having an extensive range for selecting the scattering factor and no need for shape parameter selection. PHSs is a good choice for modeling a real-world problem with complex geometries.

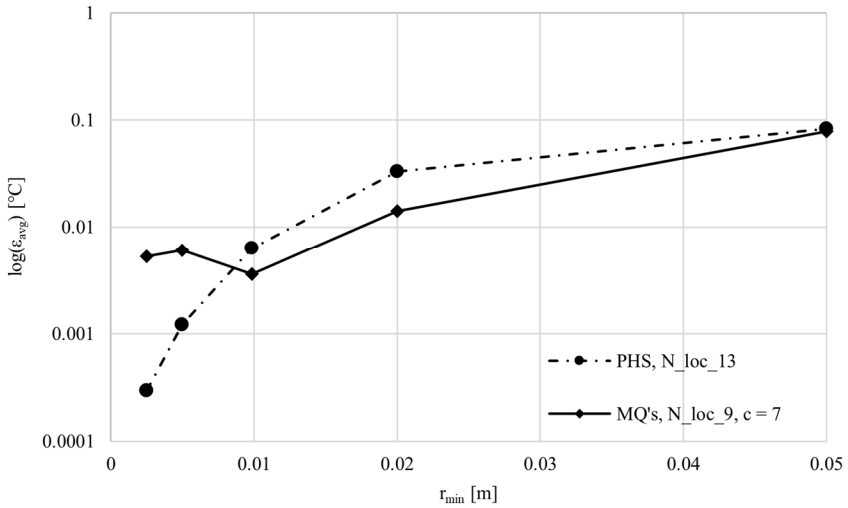

Figure 22. Case 1, ε_{avg} as a function of node distance (QUND, $\delta = 0.10$, MQ with $N_{aug} = 1$, PHS with $N_{aug} = 6$).

3.1.6. Effects of Scaling Factor on MQs

So far, we have produced all the results using scaled MQ RBFs, as shown in Equation (17). To see the effects of the scaling factor, we have carried out some simulations without the scaling factor for 9 and 13 nodes in the local subdomain for regular node arrangements ($N = 241 \times 401$), as shown in Figures 23 and 24. Figure 23 shows the effects of the shape parameter over the average error for scaled and unscaled MQs using the RND. The scaled MQ possesses a wide range for selecting shape parameters, and the average error decreases as we increase the shape parameter value, as explained earlier in Section 3.1.2. On the other hand, the unscaled MQ is sensitive to the shape parameter, and as we increase the shape parameters value, the average error rises abruptly. For local nodes $_{l}N = 9$, a wide range is available for selecting the shape parameter, but the average error increases as we increase the shape parameters value, and the results diverge as we reach a value of 40 for the shape parameter. If the local nodes are expanded to $_{l}N = 13$, then the range for selecting the shape parameter gets limited to a maximum value of two, and the average error overshoots as we increase the shape parameter from one to two.

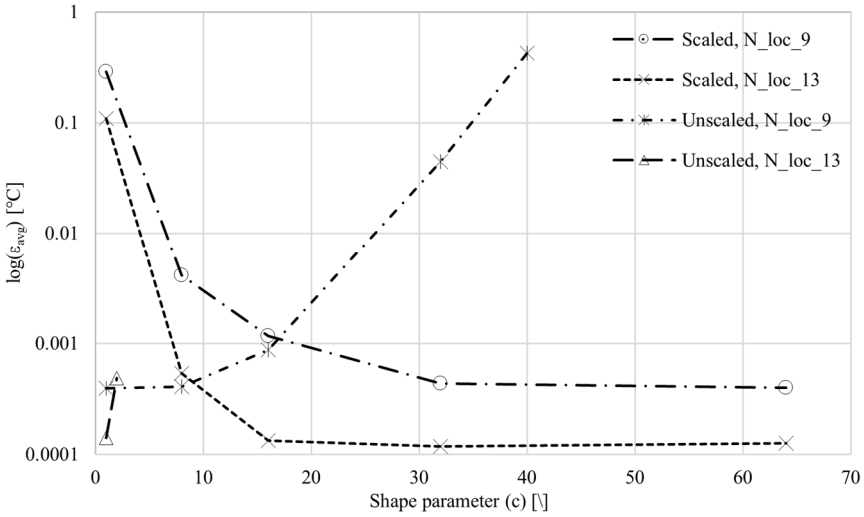

Figure 23. Case 1, ε_{avg} as a function of the shape parameter (c) for scaled and unscaled MQs (RND, $N = 241 \times 401$).

Figure 24 shows that the scattering factor impacts the unscaled MQ much more than the scaled MQ. For the unscaled MQ, a shape parameter equal to 1 leads to a divergence of the results, even with a scattering factor as low as 0.001. Based on the outcomes of Figure 23, we used the shape parameter equal to 0.08 in the simulations for the unscaled MQ with QUNDs in Figure 24. It is evident from Figure 24 that the scaled MQ provides stable results for a much larger scattering factor than the unscaled MQ. In addition, we have used shape parameters 7 and 2 with local nodes 9 and 13, respectively, because from Figure 19, we know that the scaled MQ with 9 and 13 local nodes has the smallest range for selecting the scattering factor with shape parameters 7 and 2, respectively.

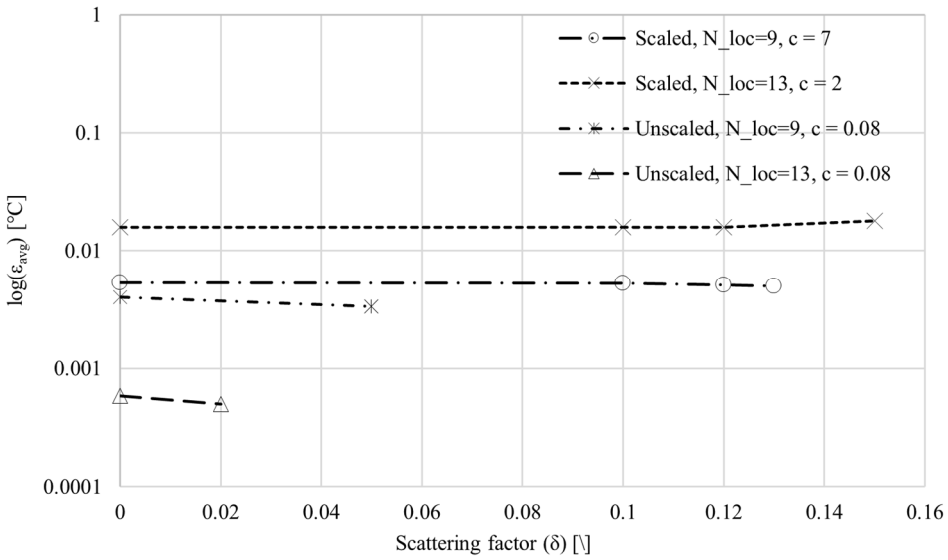

Figure 24. Case 1, ε_{avg} as a function of the scattering factor (δ) for scaled and unscaled MQs (QUND, $N = 241 \times 401$).

3.2. Results and Discussion for Case 2

3.2.1. Analysis of MQs for Different Parameters and Total Time [s]

The detailed results of the average temperature error using MQs are shown graphically in Figures 25–27.

Figure 25 shows the average temperature error [°C] as a function of the node distance [m], demonstrating the impact of gradually increasing the total time. As the total time progresses from t = 0.001 [s], t = 0.01 [s], t = 0.1 [s], to t = 1 [s], it is evident that the average temperature error consistently decreases. This trend holds true while keeping the shape parameter and the number of nodes in the local subdomain constant. This behavior is due to the fact that, as the total time increases, the numerical simulation undergoes more timesteps, allowing for better stabilization and a reduction in transient effects. Consequently, the solution tends towards a steady state that is flat everywhere, resulting in increasingly minor average temperature errors.

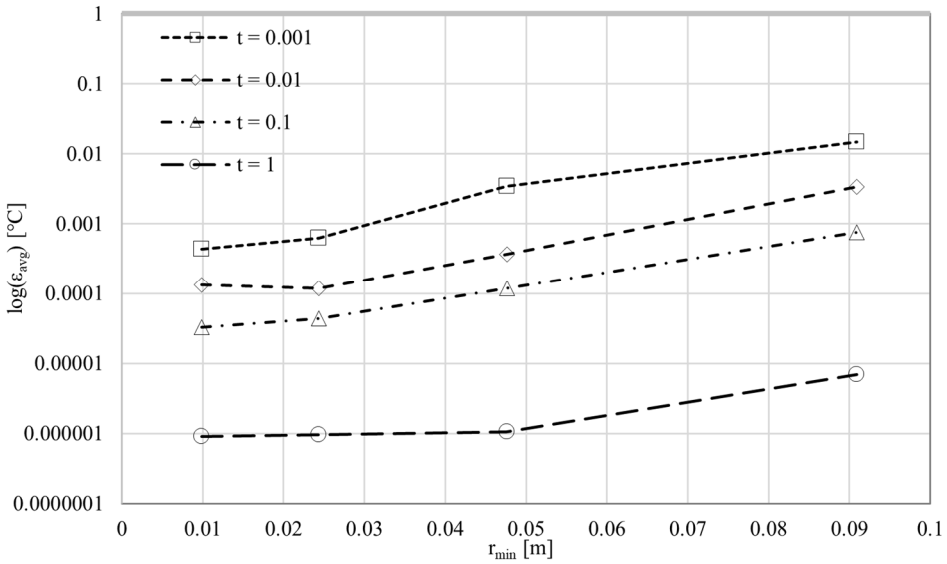

Figure 25. Case 2, MQ, ε_{avg} as a function of node distance for four different times (RND, $N_{aug}=1$, ${}_{l}N=13$, c = 32).

Figure 26 shows that the accuracy of the results improves by increasing the number of nodes in the local subdomain by keeping the same shape parameter and total time as long as the results converge. In the case of 25 nodes in the local subdomain, the results diverge if we use a large shape parameter (8, 16, 32). That is why the results are not shown in Figure 26 for the case with 25 nodes in the local subdomain.

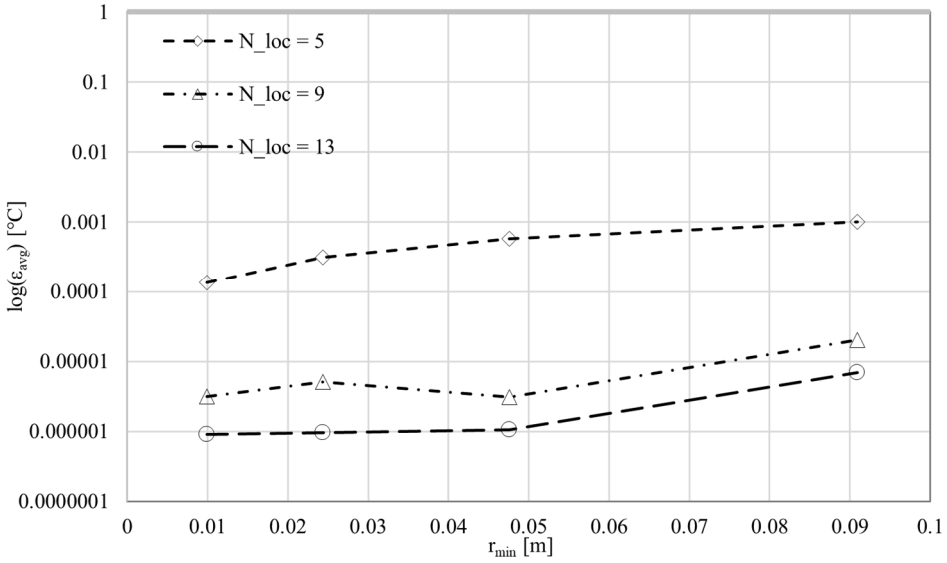

Figure 26. Case 2, MQ, ε_{avg} as a function of node distance for three different ${}_{l}N$ (RND, $N_{aug}=1$, c = 32, t = 1 s).

While we have already carried out a detailed analysis for finding the optimal shape parameter with different nodes in the local subdomain in Section 3.1.2, to compare the results for the time-dependent case, we show the results for all the optimal shape parameters with the respective number of nodes in the local subdomain in Figure 27. From Figure 27, we can conclude that the accuracy of the results increases by increasing the number of nodes in the local subdomain and using the optimal shape parameter (c).

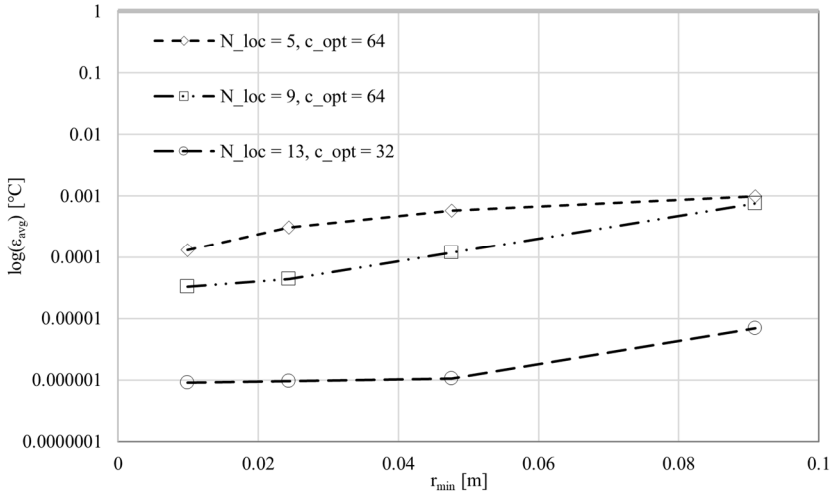

Figure 27. Case 2, MQ, ε_{avg} as a function of node distance for four different ${}_lN$ with optimal shape parameters (RND, $N_{aug}=1$, t = 1 s).

3.2.2. Analysis of PHSs for Different Parameters and Total Time [s]

A similar trend to the MQs can be seen while using PHSs with different maximum times; if we increase the total time, then the accuracy of the results improves, provided the number of nodes in the local subdomain remains constant, as shown in Figure 28 (${}_lN=9$), Figure 29 (${}_lN=13$), and Figure 30 (${}_lN=25$) respectively. This improvement is a logical consequence of the fact that the analytical and numerical solutions tend to a flat constant value.

The only exception in PHS simulations arises when employing five nodes in the local subdomain. In this case, a singular matrix is encountered, leading to the termination of the simulation. Also, according to [24], to obtain stable results, the number of nodes in the local subdomain should be at least double the number of augmentation, i.e., in our case, as we used $N_{\text{aug}}=6$, so if we use ${}_lN$ greater than or equal to 12, then we will obtain stable and converging results. Therefore, PHSs will never work while using five nodes in the local subdomain with $N_{\text{aug}}=6$ because when ${}_lN \le N_{\text{aug}}$, then the matrix will become singular due to the appearance of one whole row equal to zero.

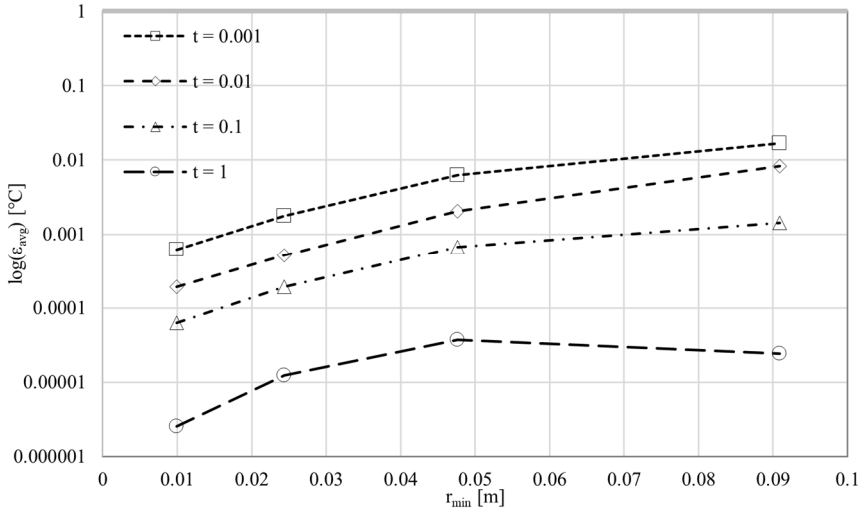

Figure 28. Case 2, PHS, ε_{avg} as a function of node distance for four different times (RND, $N_{aug}=6$, ${}_lN=9$).

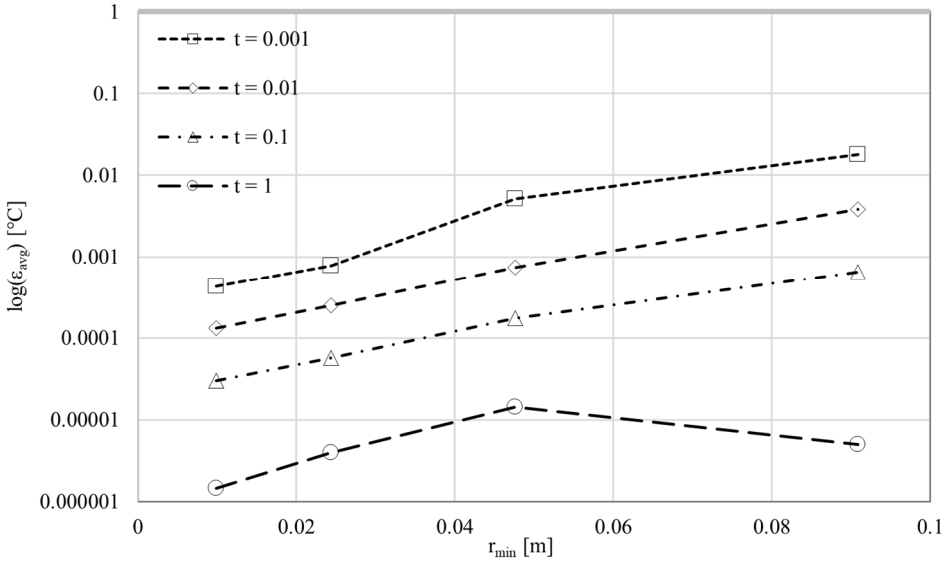

Figure 29. Case 2, PHS, ε_{avg} as a function of node distance for four different times (RND, $N_{aug} = 6$, ${}_{l}N = 13$).

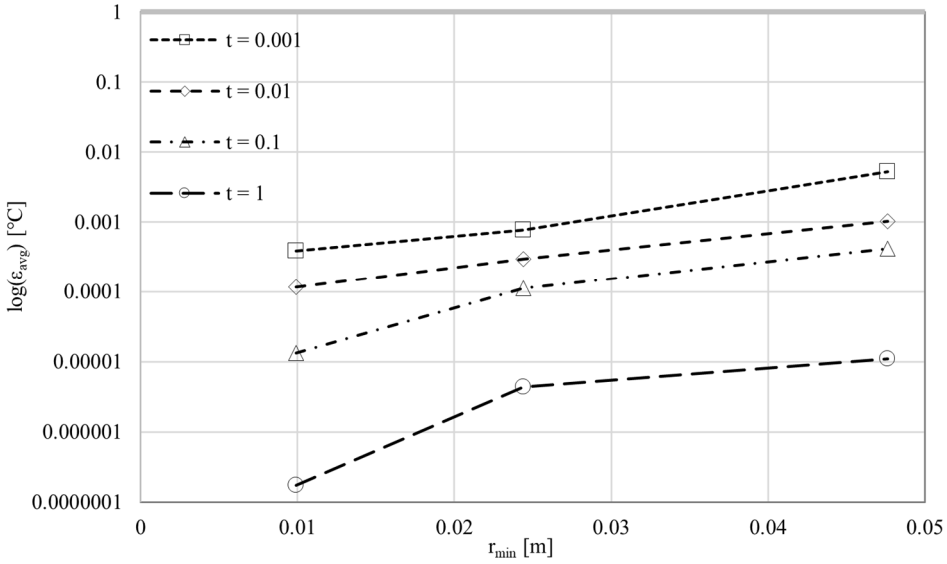

Figure 30. Case 2, PHS, ε_{avg} as a function of node distance for four different times and three node arrangements (RND, $N_{aug} = 6$, ${}_{l}N = 25$).

From Figure 31, it can be concluded again that the results are more accurate for PHSs if we increase the number of nodes in the local subdomain.

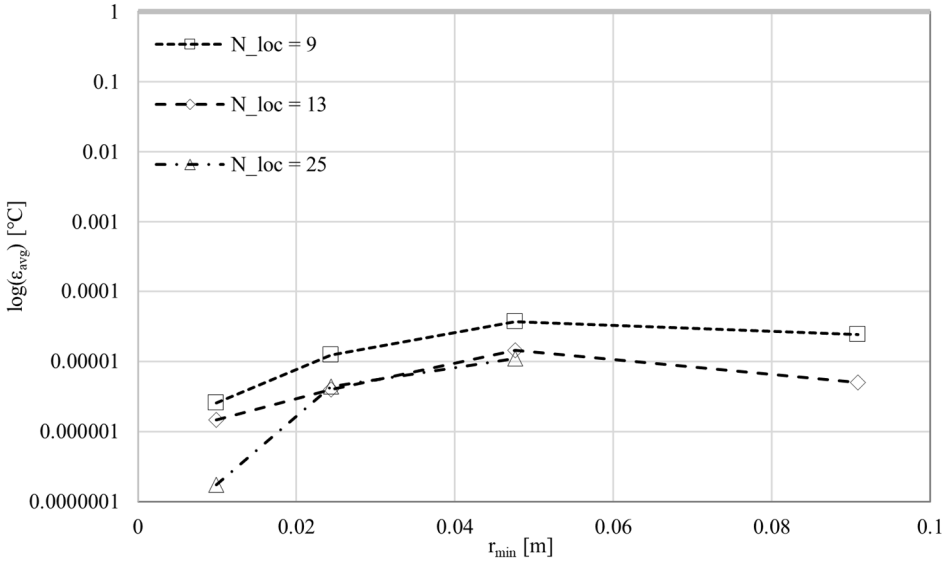

Figure 31. Case 2, PHS, ε_{avg} as a function of node distance for three different ${}_{l}N$ (RND, $N_{aug} = 6$, t = 1 s,).

Figure 32 compares MQs and PHSs based on the average temperature error as a function of node distance. We can see that using MQs produce more accurate results than PHSs.

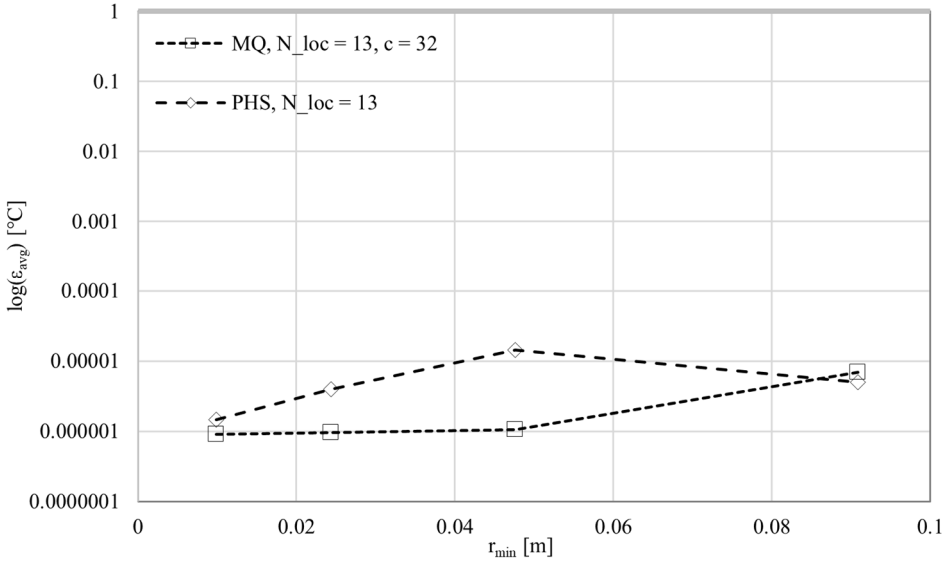

Figure 32. Case 2, comparison of MQ ($N_{aug} = 1$) and PHS ($N_{aug} = 6$) in terms of ε_{avg} as a function of node distance (RND, ${}_{l}N = 13$, t = 1 s).

4. Discussion

This paper compares LRBFCMs, structured with MQs and PHSs◎shape functions, for solving the HDE. The present research represents a follow-up of our previous pioneering publication on LRBFCM [5], based only on MQs, by comparing MQs and PHSs with a detailed assessment of how the factors such as node density, timestep, shape parameter, scaling of the MQ, number of nodes in the local subdomain, augmentation, and irregular node arrangements affect the average error in the discussed boundary value and initial value test cases.

In Case 1 studies, we can see that using augmentation leads to improved accuracy, as shown in Figure 10. In addition, this study shows that using a constant or a linear polynomial as the augmentation for MQs produces the same average temperature error, as shown in Figure 11. In addition to this, a comprehensive investigation was carried out to determine the optimal shape parameter for the MQs using various numbers of nodes within the local subdomain (Figures 12 and 14) as well as various node densities (Figures 13 and 15). We have conducted our simulations for a range of shape parameters ($c = 1,8,16,32,64$) and assessed the accuracy of the results based on the average temperature error.

In Case 1 of this study, for the scaled MQ, we found that the number of nodes in the local subdomain affects the selection of the shape parameter (explained in 3.1.2). When fewer nodes are in the local subdomain, we have a wide range of choices for the shape parameter. In this situation, using a larger shape parameter can help to improve accuracy as long as the results stay stable. Conversely, with more nodes in the local subdomain, our range of choices for the shape parameter becomes smaller to ensure the stability of the simulation. Therefore, picking a suitable shape parameter for MQs is crucial. The sensitivity analysis of MQs based on the scaling factor was also studied. It was shown that a MQ without scaling is extremely sensitive to the shape parameter (Figure 23) and scattering factor (Figure 24). Therefore, it is recommended to use a scaled MQ for better stability and accuracy.

PHS and MQ exhibit converging behavior with increasing node density (as shown in Figure 16 and Figure 17, respectively). We conducted a comparative analysis to assess the accuracy of both MQs and PHSs using the RND (as depicted in Figure 18). The highest accuracy for both MQs and PHSs was achieved with 13 nodes in the local subdomain. The findings indicate that MQs and PHSss delivered similar accuracy at lower node densities. Nevertheless, MQs demonstrated superior accuracy at higher node densities compared to PHSs.

In PHSs, node irregularity has a smaller impact on the results, enabling QUNDs more widely than MQs (as shown in Figure 19). For both PHSs and MQs, the selection of the number of nodes in the local subdomain is significantly affected by the scattering of the nodes. If the number of nodes in the local subdomain is small, then the maximum value for the scattering factor (δ) should be small too for stable results. The available range for the possible values of the scattering factor is inversely related to the shape parameter. A small shape parameter provides a wide range for choosing the scattering factor and vice versa. The MQ shows higher accuracy for less dense QUNDs; however, PHSs produce more accurate results if the nodes are denser. A higher convergence rate is observed for PHSs than MQs with scattered node arrangements, as shown in Figure 22. For comparison with QUND, we selected the most accurate results (from Figures 20 and 21) for both MQs and PHSs based on the number of nodes in the local subdomain. The conclusion was that MQs performs better with a lower node density, while PHSs provide better accuracy when the node density is high (Figure 22).

The results of Case 2 for both MQs and PHSs are studied based on the number of nodes in the local subdomain ($_lN = 5,9,13,25$), total computational time ($t[\mathrm{s}] = 0.001, 0.01, 0.1, 1$), and different node densities with optimal shape parameters using RNDs. The comparative analysis of PHSs and MQs was repeated using a different number of nodes in the local subdomain as the basis (Figure 32). The results reconfirmed that the MQ demonstrates higher accuracy than PHSs, as previously observed in the Case 1 study. MQs and PHSs individually produce more accurate results with the increasing number of nodes in the local subdomain. It is also observed that for PHSs, the number of nodes in the local subdomain should be at least greater than or equal to twice the number of the augmentation. Meanwhile, the MQ does not require any such conditions. The simulation results indicate that implementing an 11 × 11 node arrangement and 25 nodes in the local subdomain is unsuccessful due to the inadequate number of nodes (Figure 30).

In conclusion, the case study analysis indicates that the MQ exhibits slightly improved accuracy for regular node arrangements compared to PHSs. On the other hand, when node arrangements are scattered, the PHS tends to produce more accurate results. PHS is more beneficial for problems that require non-uniform node arrangements. In Case 1 of our study, we found that when comparing the best results achieved using QUND, with a scattering factor of 0.10 (as depicted in Figure 22) and RND (shown in Figure 18) for PHSs and MQs, the average accuracy difference (considering all the node arrangements used in this study) for PHS is only 0.41%. However, for MQ, this difference is considerably larger at 11.24%. Additionally, the PHS does not require finding an optimal shape parameter, making it more practical and efficient than MQ for solving real-world problems. In the future, we recommend using PHSs for practical purposes and longer robustness in QUND.

Author Contributions: Conceptualization B.Š.; software I.A. and R.V.; validation, I.A. and R.V.; writing—original draft preparation, I.A.; writing—review and editing, B.Š. and U.H.; visualization I.A.; supervision U.H. and B.Š.; project administration, B.Š.; funding acquisition, B.Š. All authors have read and agreed to the published version of the manuscript.

Funding: The Slovenian Research and Innovation Agency has supported this work in the framework of the Young Researcher Program (I.A.), program group P2-0162 (B.Š and R.V), project L2-2609 (U.H.), projects L2-3173 and J2-4477 (B.Š.), and Štore-Steel Company (www.store-steel.si).

Data Availability Statement: Data will be made available on request.

Acknowledgments: The authors would like to thank Dr. Vanja Hatić for useful discussions.

Conflicts of Interest: The authors declare no conflicts of interest to this work.

References

1. Glicksman, M.E. *Diffusion in Solids: Field Theory, Solid-State Principles, and Applications*; John Wiley & Sons, Inc.: Hoboken, NJ, USA, 1999.
2. Bocquet, J.L.; Brebec, G.; Limoge, Y. Diffusion in metals and alloys. In *Physical Metallurgy*; Elsevier Science BV: Amsterdam, The Netherlands, 1996; pp. 535–668.
3. Shewmon, P. *Diffusion in Solids*, 2nd ed.; The Minerals, Metals and Materials Society: Pittsburgh, PA, USA, 2016.
4. Liu, G.R.; Gu, Y.T. *An Introduction to Meshfree Methods and Their Programming*; Springer: Dordrecht, The Netherlands, 2005.
5. Šarler, B.; Vertnik, R. Meshfree explicit local radial basis function collocation method for diffusion problems. *Comput. Math. Appl.* **2006**, *51*, 1269–1282.
6. Pepper, D.W.; Kassab, A.J.; Divo, E.A. *An Introduction to Finite Element, Boundary Element, and Meshless Methods with Applications to Heat Transfer and Fluid Flow*; American Society of Mechanical Engineers: New York, NY, USA, 2014.
7. Rabczuk, T.; Song, J.H.; Zhuang, X.; Anitescu, C. *Extended Finite Element and Meshfree Methods*; Academic Press is an imprint of Elsevier: London, UK, 2020.
8. Griebel, M.; Schweitzer, M.A. *Meshfree Methods for Partial Differential Equations, Lecture Notes in Computational Science and Engineering*; Springer: Berlin, 2003; Volume 26.
9. Chen, Y.; Lee, J.D.; Eskandarian, A. *Meshless Methods in Solid Mechanics*; Springer: New York, NY, USA, 2006.
10. Ferreira, A.J.M.; Kansa, E.J.; Fasshauer, G.E.; Leitao, V.M.A. *Computational Methods in Applied Science, Progress on Meshless Methods*; Springer: Barcelona, Spain, 2009.
11. Kansa, E.J. Multiquadrics—A scattered data approximation scheme with applications to computational fluid-dynamics—II solutions to parabolic, hyperbolic and elliptic partial differential equations. *Comput. Math. Appl.* **1990**, *19*, 147–161.
12. Kansa, E.J. Multiquadrics—A scattered data approximation scheme with applications to computational fluid-dynamics—I surface approximations and partial derivative estimates. *Comput. Math. Appl.* **1990**, *19*, 127–145.
13. Kosec, G.; Šarler, B. H-adaptive local radial basis function collocation meshless method. *Comput. Mater. Contin.* **2011**, *26*, 227–253.
14. Mavrič, B.; Šarler, B. Local radial basis function collocation method for linear thermoelasticity in two dimensions. *Int. J. Numer. Methods Heat Fluid Flow* **2015**, *25*, 1488–1510.
15. Mavrič, B.; Sarler, B. Equivalent-PDE based stabilization of strong-form meshless methods applied to advection-dominated problems. *Eng. Anal. Bound. Elem.* **2020**, *113*, 315–327.
16. Mramor, K.; Vertnik, R.; Šarler, B. Simulation of laminar backward facing step flow under magnetic field with explicit local radial basis function collocation method. *Eng. Anal. Bound. Elem.* **2014**, *49*, 37–47.
17. Hanoglu, U.; Šarler, B. Multi-pass hot-rolling simulation using a meshless method. *Comput. Struct.* **2018**, *194*, 1–14.

18. Rippa, S. An algorithm for selecting a good value for the parameter c in radial basis function interpolation. *Adv. Comput. Math.* **1999**, *11*, 193–210.
19. Mavric, B. Meshless Modeling of Thermo-Mechanics of Low-Frequency Electromagnetic Direct Chill Casting. Ph.D. Thesis, University of Nova Gorica, Rožna Dolina, Slovenia, 2017.
20. Mohammadi, V.; Dehghan, M. A POD-RBF-FD scheme for simulating chemotaxis models on surfaces. *Eng. Anal. Bound. Elem.* **2022**, *143*, 316–330.
21. Mohammadi, V.; Dehghan, M.; Marchi, S.D. Numerical simulation of a prostate tumor growth model by the RBF-FD scheme and a semi-implicit time discretization. *J. Comput. Appl. Math.* **2021**, *388*, 113314.
22. Wang, F.; Chen, Z.; Li, P.; Fan, C. Localized singular boundary method for solving Laplace and Helmholtz equations in arbitrary 2D domains. *Eng. Anal. Bound. Elem.* **2021**, *129*, 82–92.
23. Fu, Z.; Tang, Z.; Xi, Q. Localized collocation schemes and their applications. *Acta Mech. Sin.* **2022**, *38*, 422167.
24. Flyer, N.; Fornberg, B.; Bayona, V.; Barnett, G.A. On the role of polynomials in RBF-FD approximations: I. Interpolation and accuracy. *J. Comput. Phys.* **2016**, *321*, 21–38.
25. Bayona, V.; Flyer, N.; Fornberg, B.; Barnett, G.A. On the role of polynomials in RBF-FD approximations: II. Numerical solution of elliptic PDEs. *J. Comput. Phys.* **2017**, *332*, 257–273.
26. Oruc, O. A radial basis function finite difference (RBF-FD) method for numerical simulation of interaction of high and low frequency waves: Zakharov–Rubenchik equations. *Appl. Math. Comput.* **2021**, *394*, 16.
27. Dobravec, T.; Mavrič, B.; Zahoor, R.; Šarler, B. A coupled domain–boundary type meshless method for phase-field modelling of dendritic solidification with the fluid flow. *International journal of numerical methods for heat & fluid flow*, **2023,** *33*, 2963-2981. .
28. Vuga, G.; Mavrič, B.; Šarler, B. An improved local radial basis function method for solving small-strain elasto-plasticity. *Comput. Methods Appl. Mech. Eng.* **2024**, *418*, 116501.
29. Vuga, G.; Mavrič, B.; Šarler, B. A hybrid radial basis function-finite difference method for modelling two-dimensional thermo-elasto-plasticity, Part 1: Method formulation and testing. *Eng. Anal. Bound. Elem.* **2024**, *159*, 58–67.
30. Vuga, G.; Mavrič, B.; Hanoglu, U.; Šarler, B. A hybrid radial basis function-finite difference method for modelling two-dimensional thermo-elasto-plasticity, Part 2: Application to cooling of hot-rolled steel bars on a cooling bed. *Eng. Anal. Bound. Elem.* **2024**, *159*, 331–341.
31. Dobravec, T.; Mavric, B.; Šarler, B. Reduction of discretization-induced anisotropy in the phase-field modelling of dendritic growth by meshless approach. *Comput. Mater. Sci.* **2020**, *172*, 109–166.
32. Bayona, V.; Flyer, N.; Fornberg, B. On the role of polynomials in RBF-FD approximations: III. Behavior near domain boundaries. *J. Comput. Phys.* **2019**, *380*, 378–399.
33. Mramor, K.; Vertnik, R.; Šarler, B. Development of Three-Dimensional LES Based Meshless Model of Continuous Casting of Steel. *Metals* **2022**, *12*, 1750.
34. Recktenwald, G.W. Finite-difference approximations to the heat equation. *Mech. Eng.* **2004**, *10*, 1–27.
35. Hatič, V.; Mavrič, B.; Šarler, B. Simulation of macrosegregation in direct-chill casting—A model based on meshless diffuse approximate method. *Eng. Anal. Bound. Elem.* **2020**, *113*, 191–203.
36. Hatič, V.; Mavrič, B.; Šarler, B. Meshless simulation of a lid-driven cavity problem with a non-Newtonian fluid. *Eng. Anal. Bound. Elem.* **2021**, *131*, 86–99.
37. Carlson, R.E.; Foley, T.A. The parameter R^2 in multiquadric interpolation. *Comput. Math. Appl.* **1991**, *21*, 29–42.
38. Golberg, M.A.; Chen, C.S.; Karur, S.R. Improved multiquadric approximation for partial differential equations. *Eng. Anal. Bound. Elem.* **1996**, *18*, 9–17.